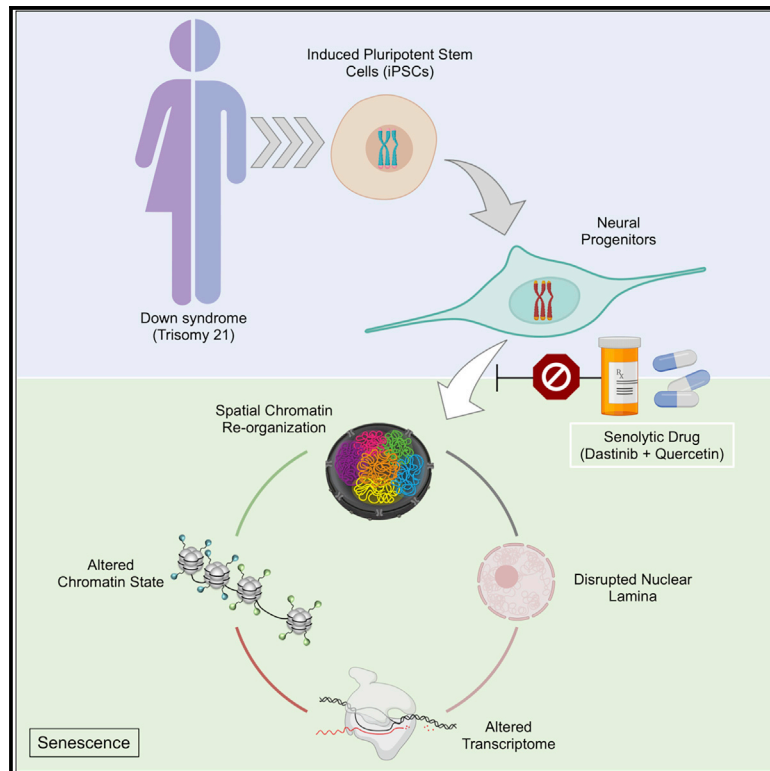


Down-syndrome-induced senescence disrupts the nuclear architecture of neural progenitors

Graphical abstract



Authors

Hiruy S. Meharena, Asaf Marco,
Vishnu Dileep, ...,
Malvina Papanastasiou,
Jacob D. Jaffe, Li-Huei Tsai

Correspondence

hiruym@mit.edu (H.S.M.),
lhtsai@mit.edu (L.-H.T.)

In brief

In this issue of *Cell Stem Cell*, Meharena et al. (2021) show that Down syndrome or trisomy 21 disrupts the 3D-genome, epigenome, and transcriptome of neural progenitors similar to that observed in senescent cells and find that the senolytic drug combination of dasatinib and quercetin ameliorates these disruptions.

Highlights

- Trisomy 21 disrupts nuclear architecture and transcriptome of neural progenitors
- Trisomy 21 harboring neural progenitors display signatures of cellular senescence
- Senolytic drugs ameliorate trisomy-21-associated molecular and cellular dysfunctions



Article

Down-syndrome-induced senescence disrupts the nuclear architecture of neural progenitors

Hiruy S. Meharena,^{1,2,*} Asaf Marco,^{1,2} Vishnu Dileep,^{1,2} Elana R. Lockshin,^{1,2} Grace Y. Akatsu,^{1,2} James Mullahoo,³ L. Ashley Watson,^{1,2} Tak Ko,¹ Lindsey N. Guerin,^{1,2} Fatema Abdurrob,^{1,2} Shruthi Rengarajan,¹ Malvina Papanastasiou,³ Jacob D. Jaffe,³ and Li-Huei Tsai^{1,2,3,4,*}

¹Picower Institute for Learning and Memory, Massachusetts Institute of Technology, Cambridge, MA 02139, USA

²Department of Brain and Cognitive Sciences, Massachusetts Institute of Technology, Cambridge, MA 02139, USA

³Broad Institute of MIT and Harvard, Cambridge, MA 02142, USA

⁴Lead contact

*Correspondence: hiruym@mit.edu (H.S.M.), lhtsai@mit.edu (L.-H.T.)

<https://doi.org/10.1016/j.stem.2021.12.002>

SUMMARY

Down syndrome (DS) is a genetic disorder driven by the triplication of chromosome 21 (T21) and characterized by a wide range of neurodevelopmental and physical disabilities. Transcriptomic analysis of tissue samples from individuals with DS has revealed that T21 induces a genome-wide transcriptional disruption. However, the consequences of T21 on the nuclear architecture and its interplay with the transcriptome remain unknown. In this study, we find that unlike human induced pluripotent stem cells (iPSCs), iPSC-derived neural progenitor cells (NPCs) exhibit genome-wide “chromosomal introversion,” disruption of lamina-associated domains, and global chromatin accessibility changes in response to T21, consistent with the transcriptional and nuclear architecture changes characteristic of senescent cells. Treatment of T21-harboring NPCs with senolytic drugs alleviates the transcriptional, molecular, and cellular dysfunctions associated with DS. Our findings provide a mechanistic link between T21 and global transcriptional disruption and indicate that senescence-associated phenotypes may play a key role in the neurodevelopmental pathogenesis of DS.

INTRODUCTION

Down syndrome (DS) is a genetic disorder caused by the triplication of chromosome 21 (T21) and is the leading cause of intellectual disability associated with abnormal brain morphogenesis (Benda, 1940; Down, 1995; Pinter et al., 2001; Weijerman and de Winter, 2010). These brain abnormalities have been associated with dysfunctional neural progenitor cells (NPCs), the multipotent stem cells of the developing brain that differentiate into neurons, astrocytes, or oligodendrocytes (Stagni et al., 2018; Tyler and Haydar, 2013). Recent whole-genome transcriptional profiling of various tissue samples from individuals with DS and DS mouse models revealed that T21 induces genome-wide transcriptional disruption in addition to the dosage-dependent upregulation of a subset of expressed genes on chromosome 21, similar to those observed in other whole-chromosome aneuploidies (Bianco et al., 2016; Dürbaum et al., 2014; FitzPatrick et al., 2002; Gonzales et al., 2018; Lejeune et al., 1959; Letourneau et al., 2014; Olmos-Serrano et al., 2016; Sheltzer et al., 2012; Tyler and Haydar, 2013; Walus et al., 2016; Wangsa et al., 2019). However, the mechanisms by which T21 induces genome-wide transcriptional disruption remain unknown.

Epigenetic modifications of chromatin determine TF-binding site accessibility at gene promoters and regulatory elements,

and the folding of chromatin within the interphase nucleus brings these two regions into spatial proximity (McLaughlin et al., 2019; Pombo and Dillon, 2015). This three-dimensional (3D) genome organization of gene promoters and regulatory elements determines the transcriptional levels of specific genes within a cell (Schoenfelder and Fraser, 2019). However, the influence of T21 on the 3D-genome organization and the role of the epigenome in the global transcriptional disruption observed in DS remain unexplored.

To explore the consequences of T21 on the molecular and cellular changes observed in DS, we established human-derived induced pluripotent stem cells (iPSCs) and iPSC-derived forebrain NPCs from multiple individuals and investigated the consequences of T21 on the 3D-genome organization, epigenome, and transcriptome (Buenrostro et al., 2013; Chambers et al., 2009; Rao et al., 2014; Topol et al., 2015; Weick et al., 2013). Our findings show that T21 induces chromosomal introversion, disrupts lamina-associated domains (LADs), and alters the genome-wide chromatin accessibility of NPCs but not iPSCs. While the overall organization of A/B compartments is conserved in NPCs harboring T21, we observed global loss of chromatin accessibility within the A-compartment that is associated with transcriptional downregulation and increased long-range chromatin interactions in the B-compartment associated with transcriptional upregulation. We find that these architectural

changes are similar to those observed in senescent cells, and our transcriptional analysis confirms that differentially expressed genes (DEGs) identified in NPCs harboring T21 are highly correlated with DEGs identified in oxidative stress-induced senescent cells. Finally, we demonstrate that the senolytic drug combination of dasatinib and quercetin (DQ) alleviates the genome-wide transcriptional disruption as well as deficits in cellular proliferation and migration observed in NPCs harboring T21.

RESULTS

T21 induces chromosomal introversion in NPCs

To determine the consequences of T21 on the global 3D-genome organization, we performed chromosome conformation capture (Hi-C) on an isogenic pair (euploid: Iso-E and trisomic: Iso-T) of iPSCs and NPCs (Maclean et al., 2012) and identified ~2.5 billion unique interactions per cell type (Figures 1A–1D; Table S1A). We first sought to interrogate the consequences of T21 on the 3D-genome reorganization that occurs during differentiation of iPSCs to NPCs. We observed significant gain and loss of both *cis*- and *trans*-chromosomal interactions in Iso-E NPCs compared with iPSCs (Figure 1E); however, in Iso-T, we observed significant genome-wide reduction of *trans*-chromosomal interactions in NPCs compared with iPSCs (Figure 1F). While T21 minimally impacted global *trans*-chromosomal interactions in iPSCs (Iso-E = 19.82% ± 1.0% and Iso-T = 21.72% ± 2.8%, *p* value = 3.4×10^{-1}) (Figures S1A and S1B), we observed a significant decrease in the fraction of *trans*-chromosomal interactions in NPCs harboring T21 (Iso-E = 21.55% ± 0.8% and Iso-T = 15.85% ± 1.2%, *p* value = 2.2×10^{-3}) (Figures 1G and 1H; Table S1B). To evaluate whether the altered distribution of chromosomal interactions induced by T21 in NPCs is conserved across individuals with DS, we derived NPCs from an additional pair of male individuals with euploid (Ma-E) and trisomic (Ma-T) karyotypes (Figure S1C). Consistent with our findings from the isogenic pair, we observed that NPCs harboring T21 exhibit reduced *trans*-chromosomal interactions compared with euploid NPCs (Figures S1D and S1E). As expected, we observed increased signal from chromosome 21 (HSA21) in both iPSCs and NPCs because of its triplication; however, when normalized for the number of chromosomes, we observed that loss of *trans*-chromosomal interactions in NPCs is distributed across all chromosomes, including HSA21 (Figure S1F; Table S1C).

T21 NPCs exhibited reduced longer-range interactions (>~1 Mb) and increased shorter-range interactions (<~1 Mb), whereas in the isogenic pair of iPSCs, the distribution of *cis*-chromosomal interactions remained unchanged (Figure S1I). This reduction of longer-range *cis*-chromosomal interactions and an increase in shorter-range interactions was observed across all chromosomes, including HSA21 in T21 NPCs but not iPSCs (Figures 1I–1L and S1J). On average, we observed an ~20% increase in shorter-range (<1 Mb) interactions in T21 NPCs (Table S1D). To ensure that these results were not confounded because of the normalization of T21, we repeated the analysis by removing chromosome 21 reads and found similar genome-wide chromosomal introversion in T21-NPCs (Figures S1K–S1N). In conclusion, we observed that T21 induces loss of *trans*-chromosomal interactions and increases shorter-

range (<1 Mb) *cis*-chromosomal interactions in NPCs but not in iPSCs.

T21 induces reorganization of intra-TAD interactions and chromosomal looping

The genome is organized into two compartments within the nucleus: the active (A) compartment, which is localized toward the nuclear core, and the inactive (B) compartment, which is localized toward the periphery on the nuclear lamina (Lieberman-Aiden et al., 2009). We found that T21 minimally impacts the classification of A/B compartments in both iPSCs and NPCs (Figures S2A and S2B). A/B compartments are composed of multiple self-interacting structural units of the genome known as topologically associating domains (TADs) (Dixon et al., 2012; Nora et al., 2012; Rao et al., 2014), and we identified 5,559 and 4,731 TADs in iPSCs and NPCs, respectively (Table S2A). While T21 did not impact the intra-TAD interaction density (ID) of iPSCs, the intra-TAD ID of NPCs was significantly reorganized in trisomic NPCs compared with euploid NPCs, where 1,800 (~38%) TADs had significantly higher ID and 389 (~8%) TADs had significantly reduced ID (Figures 2A–2D). Next, we performed an enrichment analysis (10 million randomized permutations) to assess whether the differentially interacting TADs preferentially localized to a specific compartment. We found that TADs with increased ID were enriched in the B-compartment, and unchanged TADs were predominantly localized in the A-compartment; however, the reduced-ID TADs were not enriched in either compartment (Figure 2E; Table S2B). While the intra-TAD ID of ~46% of TADs was significantly altered, the directionality index and insulation score remained unchanged as a consequence of T21 in both iPSCs and NPCs, indicating a general maintenance of global chromatin architecture and TAD boundaries (Figure S2C).

Next, we identified 12,053 loops in iPSCs and 11,373 loops in NPCs: of these, 2,653 and 1,973 loops are unique to iPSCs and NPCs, respectively (Figures 2F and S2D; Table S2C). Differential chromosomal looping analysis revealed that ~700 loops were significantly reduced or lost in T21 NPCs, where 27 loops were only identified in euploid NPCs (*z* score Iso-E = 17.75 and Iso-T = 0.84), and 672 were significantly reduced in T21 NPCs (*z* score Iso-E = 64.46 and Iso-T = 32.46). Conversely, we identified ~3,800 loops significantly enhanced in T21 NPCs, with 264 *de novo* loops (*z* score Iso-E = 2.19 and Iso-T = 33.97), and 3,494 significantly increased loops in T21 NPCs (*z* score Iso-E = 30.75 and Iso-T = 62.56). Additionally, enrichment analysis revealed that the chromosomal loops that were lost/reduced were predominantly localized in TADs with reduced ID (*p* value = 0.00596, 10 million randomized permutations), and the *de novo*/increased loops were enriched in TADs with increased ID (*p* value = 0.00539) (Figure 2E; Table S2B). In summary, we find that T21-induced introversion is predominantly localized within the inactive B-compartment.

Disruption of nuclear lamina is associated with increased intra-TAD interactions

The B-compartment is localized toward the nuclear periphery on the nuclear lamina and is enriched for the histone modification H3K9me3 (Shevelyov and Ulianov, 2019). To interrogate the consequences of T21 on genome organization around the nuclear lamina, we utilized immunofluorescence to label the nuclear

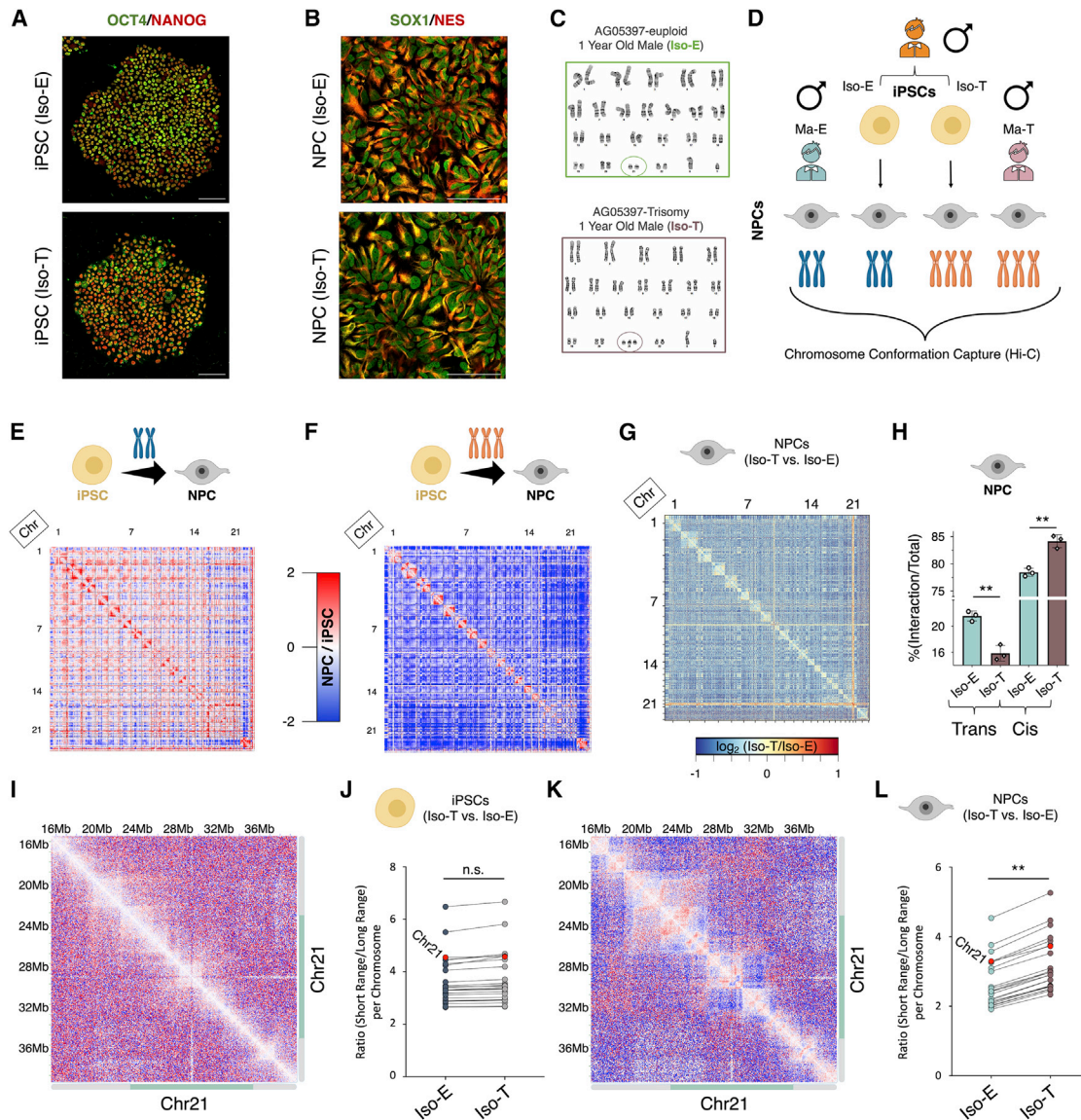


Figure 1. T21 induces genome-wide chromosomal introversion in NPCs, but not iPSCs

(A–C) Immunofluorescence staining of (A) iPSCs (OCT4 [green], NANOG [red]) and (B) NPCs (SOX1 [green], Nestin [red]) from the isogenic pair (Iso-E [top] and Iso-T [bottom]) as well as (C) respective G-band karyotyping of NPCs.

(D) Schematic of experimental design to assess the 3D-genome of the isogenic pair iPSCs and NPCs as well as the euploid (Ma-E) and trisomic (Ma-T) male NPCs.

(E–H) Comparative Hi-C analysis of Iso-E and Iso-T iPSCs and NPCs. Genome-wide differential (NPC/iPSC) Hi-C interaction maps for Iso-E (E) and Iso-T (F). (G) Genome-wide differential (Iso-T/Iso-E) Hi-C interaction maps for NPCs. (H) Percent distribution of *trans*- and *cis*-chromosomal interactions for the isogenic pair of NPCs (t test).

(I–L) Representative images of chromosome 21 (chr21) differential *cis*-chromosomal interaction maps for the isogenic pair of iPSCs (I) and NPCs (K). Dot plots representing the ratio of short-range (<1 Mb) to long-range (>1 Mb) interactions for the isogenic pair of iPSCs (J) and NPCs (L). Each dot represents a chromosome, and chr21 is represented as a red dot. Wilcoxon rank-sum test shows that euploid and trisomic iPSCs were not statistically different (p value = 0.536), whereas NPCs show significantly increased short-range interactions in the trisomic NPCs (p value = 0.004).

lamina and H3K9me3. We examined the localization of H3K9me3 and the lamina-associated protein LMNB1 to interrogate the consequences of T21 on lamina organization. While the overall architecture of the nuclear envelope and heterochromatin organization in T21 iPSCs remains unchanged (Figures S3A–S3C; Table S3A), we observed decreased levels of LMNB1 in T21 NPCs relative to the euploid NPCs (Figures 3A and 3B).

The global intensity of H3K9me3 was unchanged in both T21 iPSCs and NPCs (Figures S3C and S3D); however, we observed an increased number of H3K9me3 aggregates specifically within the nuclei of T21 NPCs and not iPSCs (Figures S3E and S3F).

To interrogate whether B-compartment TAD introversion is associated with disruption of the nuclear lamina, we performed ChIP-seq for LMNB1 in the isogenic pair of NPCs (Figure S3G).

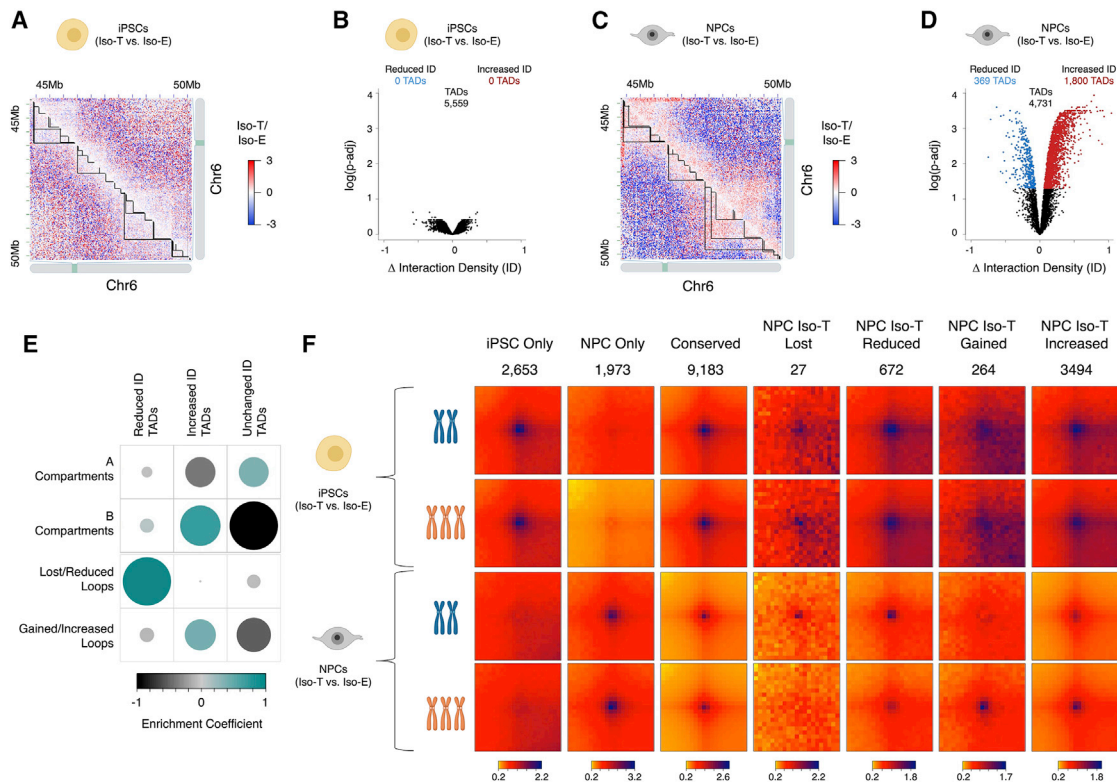


Figure 2. T21 induced reorganization of TADs and loops are segregated into A/B compartments

(A and C) Representative images of differential Hi-C interaction maps (Iso-T/Iso-E) of a region on chromosome 6 (chr6) in the isogenic pair of iPSCs (A) and NPCs (C).

(B and D) Volcano plot of differential interaction density (ID) within TADs in the isogenic pair of iPSCs (B) and NPCs (D).

(E) Randomized permutation test analysis between the differential interaction density (ID) TADs with A/B compartments and differential chromosomal loops in NPCs. Color intensity (positive correlations are displayed in green, and negative correlations in black) and the size of the circle are proportional to the enrichment coefficients of A/B compartments with differentially interacting TADs identified as a consequence of T21 in NPCs.

(F) Aggregate Peak Analysis (APA) of loops uniquely identified in iPSCs (top rows) and NPCs (bottom rows) in both Iso-E and Iso-T.

We identified 949 LADs, which are associated with ~53% of the genome, and from these, we observed a loss of ~7% of the LADs (113 Mb) and a gain of <1% (10 Mb) in T21 NPCs (Figures 3C and S3H). As expected, LAD enrichment analysis demonstrated that the A-compartment was depleted for LMNB1 association in both Iso-E and Iso-T NPCs ($r = 0.4134$) (Figure S3I), whereas the B-compartment was highly enriched for LMNB1-associated genomic regions ($r = 0.4267$) (Figure 3D; Table S3B). Additionally, LMNB1 occupancy was significantly (p value $< 10^4$) reduced in the B-compartment of Iso-T NPCs compared with that in Iso-E NPCs. Next, we sought to investigate the relationship between TAD interaction and LAD enrichment and found that TADs with increased ID have significantly lower LMNB1 enrichment than TADs with reduced ID or unchanged ID (Figures 3E and 3F and S3J–S3O; Table S3C). In conclusion, we observed reduced LMNB1 association in TADs within the B-compartment that have increased intrachromosomal interactions in Iso-T NPCs compared with Iso-E NPCs.

T21-induced transcriptional upregulation is associated with chromosomal introversion

To examine the relationship between T21-associated nuclear architecture reorganization and the transcriptome, we performed

RNA sequencing of iPSCs and NPCs derived from the isogenic pair as well as NPCs derived from individuals with DS (female [Fe-T] and male [Ma-T]) and euploid controls (female [Fe-E] and male [Ma-E]) (Figure 4A and Figure S1C). Principal component analysis showed that transcriptionally, NPCs derived from the different individuals segregate by karyotype on the first principal component (Figure S4A). We observed that T21 had a greater impact on the NPC transcriptome than the transcriptome of iPSCs: NPCs exhibited 1,869 downregulated and 2,724 upregulated DEGs (false discovery rate [FDR] < 0.01 , \log_2 fold change ≥ 0.5 or ≤ -0.5), while iPSCs exhibited 102 downregulated and 423 upregulated DEGs (Figures 4B and 4C). Comparison of the DEGs identified in NPCs derived from different individuals (pairwise comparisons of Iso-T versus Iso-E, Fe-T versus Fe-E, and Ma-T versus Ma-E) showed a significant concordance of the upregulated and downregulated genes after running 10 million randomized permutations of the expression data (Figure S4B; Tables S4A and S4B). To ensure that the transcriptional observations were not due to normalization of T21, we repeated our differential analysis of the isogenic pair after removing all reads originating from chromosome 21 and observed a similar genome-wide transcriptional disruption (Figure S4C). While both iPSCs and NPCs exhibited upregulation of ~25% of the

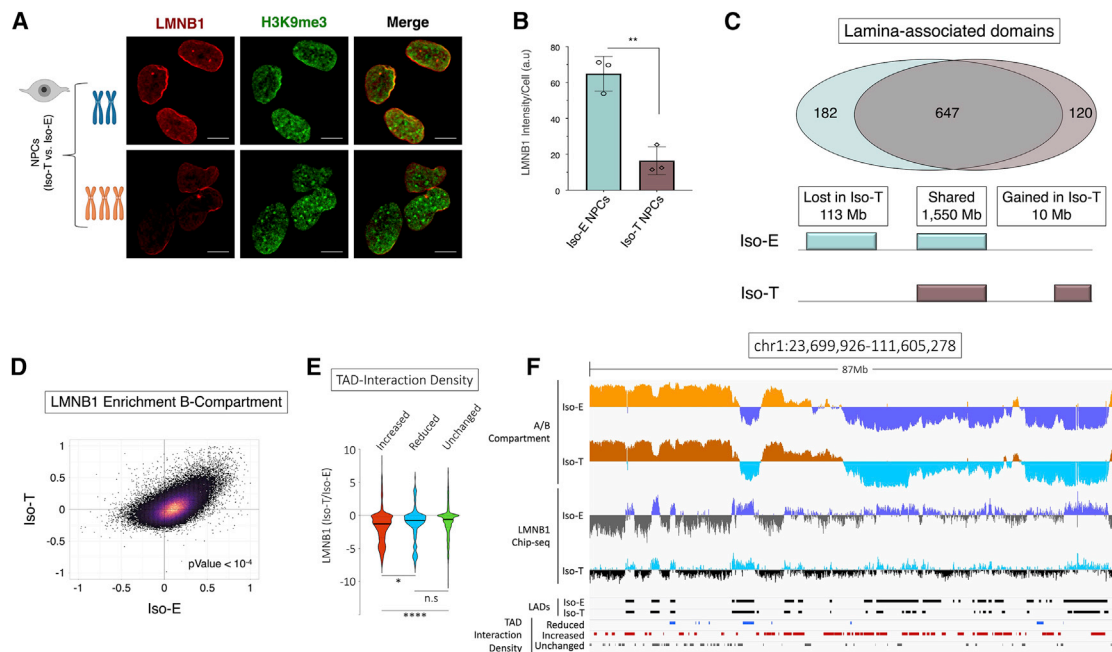


Figure 3. T21-induced disruption of lamina-associated domains (LADs) is associated with chromosomal introversion

(A) Immunofluorescence of LMNB1 (red) and H3K9me3 (green) in the isogenic pair of NPCs.

(B) Quantification of LMNB1 staining intensity in the isogenic pair of NPCs. Each dot on the histogram represents a replicate experiment of ~ 440 total nuclei analyzed for the isogenic pair of NPCs (t test).

(C) Venn diagram of LAD overlap between the euploid (Iso-E) and T21 (Iso-T) NPCs (intersect of replicates); bottom, schematic representation of genome coverage (base pairs) by LADs gained or lost as a consequence of T21 relative to euploid.

(D) Scatter plot of LMNB1 enrichment over input in Iso-E (x axis) and Iso-T (y axis) of the genomic region in the B-compartment.

(E) Violin plot of fold change of LMNB1 (Iso-T/Iso-E) of the differential (increased-ID [red], reduced ID [blue], and unchanged ID [green]) interaction density TADs. (F) IGV plot of A-compartment (Iso-E [yellow] and Iso-T [orange]) and B-compartment (Iso-E [blue] and Iso-T [light-blue]), LMNB1 ChIP-seq of Iso-E (blue) and Iso-T (light-blue), as well as the location of LADs (black) and the differentially interacting TADs (reduced ID [blue], increased ID [red], and unchanged ID [gray]), an 87 Mb region of chromosome 1.

genes expressed on HSA21, NPCs showed disruption of $\sim 20\%$ (8.5% downregulation and 11.6% upregulation) of expressed genes on all the other chromosomes. In contrast, iPSCs only exhibited alterations of $\sim 3\%$ (0.6% downregulation and 2.6% upregulation) of the expressed genes on all the other chromosomes (Figures S4D and S4E).

In both iPSCs and NPCs, we found that the A and B compartments are composed of similar genome sizes, and, as expected, the majority of expressed genes are located in the A-compartment ($\sim 80\%$ and $\sim 76\%$ of expressed genes in iPSCs and NPCs, respectively; Table S4C). However, we found that the DEGs identified in NPCs were distinctly segregated into the two compartments, with downregulated genes predominantly located in the A-compartment and upregulated genes enriched in the B-compartment (Figure 4D; Tables S4D and S4E). We found that TADs with increased interaction densities and increased looping events are enriched for upregulated genes, exhibit reduced LMNB1 association, and are predominantly located in the B-compartment (p value $< 1 \times 10^{-07}$; Figures 4E, S4F, and S4G; Tables S4F–S4H). Conversely, TADs with reduced ID in T21 NPCs are enriched for downregulated genes and are not enriched in either compartment (p value $< 1 \times 10^{-07}$). Although the A-compartment is predominantly enriched for downregulated genes, we observed that this compartment is predominantly enriched for TADs with unchanged ID (p value $<$

1×10^{-07}), suggesting that the downregulation of genes observed in the A-compartment is independent of altered long-range promoter-enhancer interactions.

We examined gene ontology by focusing on those DEGs localized within differential ID TADs and found that downregulated genes within reduced-ID TADs were enriched for brain development-associated processes, whereas upregulated genes localized within increased-ID TADs were predominantly enriched for biological processes involving cell migration, cell adhesion, and ECM organization (Figures 4F and 4G). The downregulated genes within unchanged-ID TADs were associated with transcriptional regulation and brain development (Figure 4H). In summary, upregulated genes were enriched in B-compartment TADs with increased ID, and downregulated genes were predominantly enriched in reduced-ID TADs and in the A-compartment. However, the mechanism underlying the downregulation of genes localized within unchanged-ID TADs remains unknown.

T21-induced reduction of chromatin accessibility is associated with dysfunction of nuclear processes

Our transcriptional analysis showed a significant number of the downregulated genes in T21 NPCs impact chromatin modifications on histone H3, including histone deacetylases (HDAC1 and HDAC2), polycomb-group proteins (EZH2 and EED), histone acetyltransferase (KAT2A), as well as the eukaryotic protein

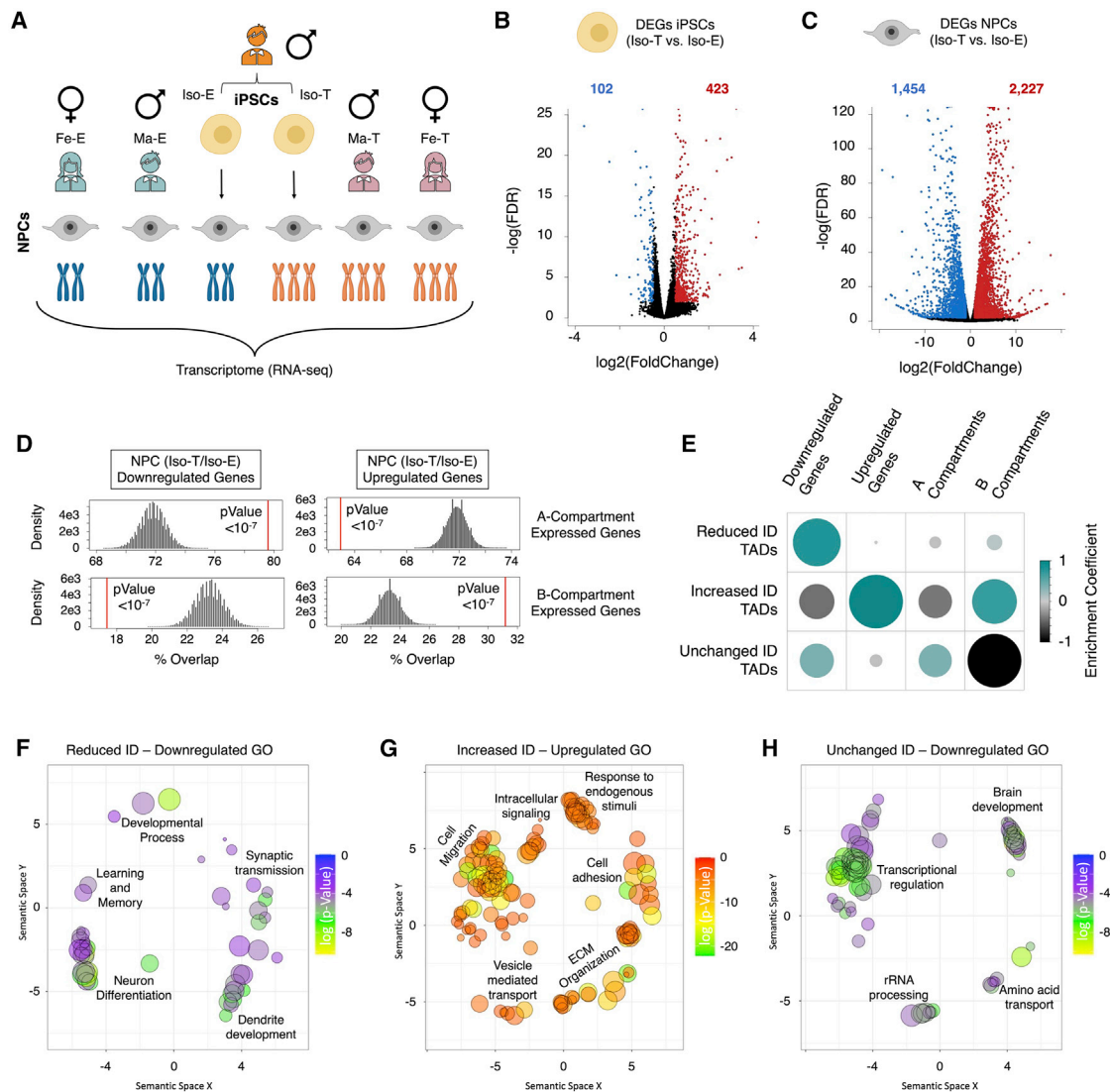


Figure 4. T21 DEGs are distinctly separated into the A/B compartments in NPCs

(A) Schematic of RNA-seq experiment on the isogenic pair (Iso-E and Iso-T) of iPSCs and NPCs as well as NPCs derived from euploid (female [Fe-E] and male [Ma-E]) and trisomic (female [Fe-T] and male [Ma-T]) individuals.

(B and C) Volcano plots of the differentially expressed genes (DEGs) identified in the isogenic pair of iPSCs (B) and NPCs.

(C and D) Randomized permutation test T21 NPC DEGs with A/B compartments. Histogram represents the range of expected overlap percentage, and the red line represents the observed percentage overlap.

(E) Corplot of the randomized permutation test between TADs with varying interaction densities (IDs) with DEGs and A/B compartments. Color intensity (positive correlations are displayed in green, and negative correlations in black) and the size of the circle are proportional to the enrichment coefficients.

(F–H) Gene ontology visualized in semantic similarity-based scatterplots for downregulated genes associated with reduced-ID TADs (F), upregulated genes associated with increased-ID TADs (G), and downregulated genes localized within unchanged-ID TADs (H).

kinases AURKB and VRK1 (Figure S5A). To assess the post-translational modification landscape of histone H3 residues, we performed global chromatin profiling (GCP), a targeted mass-spectrometry-based assay that quantifies histone post-translational modifications in bulk chromatin (Figure S5B; Table S5A) (Jaffe et al., 2013). Comparison of the isogenic pair of NPCs showed a significant reduction of the mitotic marker H3 serine-10 phosphorylation (H3S10p), consistent with previous studies indicating reduced cellular proliferation in DS (Contestabile et al., 2009; Contestabile et al., 2007; Guidi et al., 2011; Mol-

drich et al., 2009). While we did not identify any significant changes to chromatin states that typically demarcate promoters or enhancers (H3 lysine-4 mono-methylation [H3K4me] and trimethylation [H3K4me3], respectively), we observed a reduction in H3 lysine-23 acetylation (H3K23ac) and an increase in H3 lysine-27 acetylation (H3K27ac), marks associated with chromatin activity, potentially indicating a relationship between the observed genome-wide transcriptional changes and the overall chromatin state (Allis and Jenuwein, 2016; Klemm et al., 2019; Lane et al., 2014; Liu et al., 2016; Lu et al., 2015).

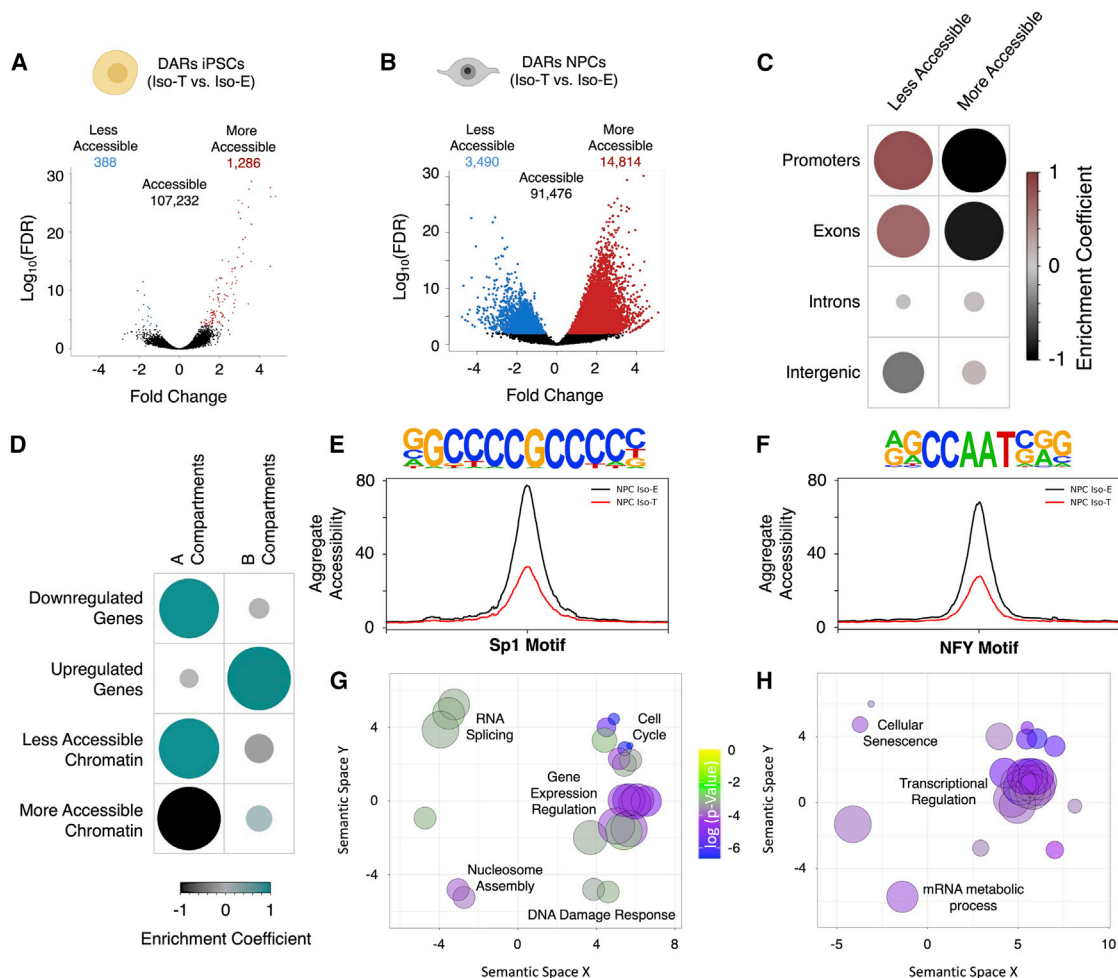


Figure 5. T21-induced genome-wide disruption of chromatin state in NPCs is associated with transcriptional downregulation

(A and B) Volcano plots of differentially accessible regions (DARs) identified by ATAC-sequencing in the isogenic pair of iPSCs (A) and NPCs (B).

(C) Enrichment heatmap of the randomized permutation test between the DARs on promoters, exons, introns, and intergenic regions with accessible regions genome wide. Color intensity (positive correlations are displayed in red, and negative correlations in black) and the size of the circle are proportional to the enrichment coefficients.

(D) Enrichment heatmap of the randomized permutation test between the A/B compartments and DEGs and DARs. Color intensity (positive correlations are displayed in green, and negative correlations in black) and the size of the circle are proportional to the enrichment coefficients of the specific genetic features with the A/B compartments.

(E and F) Aggregate plots of less accessible regions harboring SP1 (E) and NFY (F) motifs.

(G and H) Gene ontology visualized in semantic similarity-based scatterplots for downregulated genes with less accessible promoters harboring SP1 (G) and NFY (H) motifs.

To assess the consequences of T21 on the genome-wide chromatin state, we utilized the assay for transposase-accessible chromatin using sequencing (ATAC-seq) on the isogenic pair of iPSCs and NPCs (Buenrostro et al., 2013). We found that while T21 minimally impacts the chromatin state of iPSCs (~1.6% of the accessible chromatin), ~20% of the accessible chromatin is altered as a consequence of T21 in NPCs with an FDR < 0.01 (Figures 5A and 5B), a level of chromatin state alteration that has recently been observed in astroglia derived from individuals with DS (Bally et al., 2020). We identified 18,304 differentially accessible regions (DARs) in T21 NPCs (14,814 more accessible and 3,490 less accessible). As expected, due to the chromosomal triplication, HSA21 is more permissive to transposase in both T21 iPSCs and NPCs (Fig-

ures S5C and S5D). Additionally, in T21 NPCs, we observed genome-wide chromatin accessibility changes that were comparable to the distribution of DEGs across the chromosomes (Figures S4D and S4E). We verified that these changes were not an artifact of T21 by repeating the normalization and analysis in the absence of reads from chromosome 21 and observed 3,419 regions with reduced accessibility and 14,605 with increased accessibility, FDR < 0.01 (Figure S5E). As both the differential gene expression and differential accessibility analysis of NPCs indicate increased transcriptional activity in T21 NPCs (Figures 4C and 5B), we assessed whether this corresponded to an increase in nascent RNA expression by labeling nascent transcripts in live NPCs via a 5-min Ethylene uridine (EU) pulse and quantified EU-RNA fluorescence. We observed

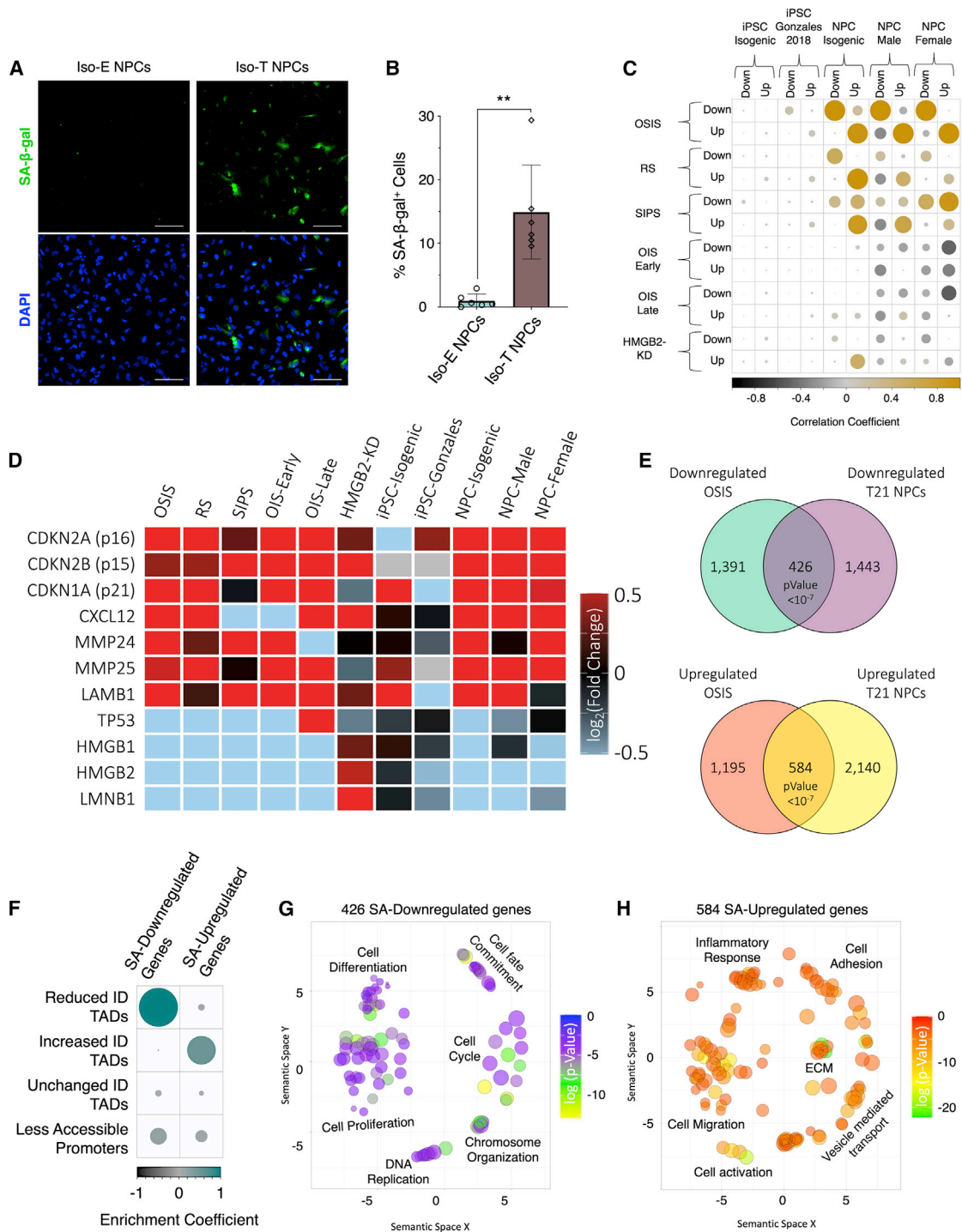


Figure 6. T21 induces senescence in NPCs

(A) Senescence-associated β-galactosidase staining (SA-β-gal, green) in euploid (left) and T21 (right) NPCs.

(B) Quantification of SA-β-gal staining intensity in the isogenic pair of NPCs. Each dot on the histogram represents a replicate experiment of ~200 cells analyzed for the isogenic pair of NPCs (t test).

(C) Correlation heatmap of the randomized permutation test of T21 iPSCs and NPC DEGs, compared with DEGs identified in various modes of senescence induction (oxidative stress-induced senescence [OSIS], replicative senescence [RS], stress-induced senescence [SIPS], early and late oncogene-induced senescence [OIS] and HMGB2 knockdown [HMGB2-KD]). Color intensity (positive correlations are displayed in yellow, and negative correlations in black) and the size of the circle are proportional to the enrichment coefficients.

(D) Gene expression heatmap of senescence marker genes as fold change of T21/E21 or senescent/control.

(legend continued on next page)

an ~20% increase in nascent RNA levels in T21 NPCs (Figures S5F and S5G; Table S5B).

To gain an understanding of the histone modifications associated with the T21 NPC DARs, we utilized published ChIP-seq data from H1-derived NPCs (Hawkins et al., 2010). While less accessible regions are equally distributed on H3K4me3, H3K4me, H3K27ac, H3K23ac, and regions not marked by any of these modifications, the more accessible regions are predominantly localized on regions with H3K4me and regions that are not marked (Figure S5H; Table S5C). However, global enrichment analysis of DARs on promoters, exons, introns, and intergenic regions (GENCODE GRCh37) revealed that less accessible regions are significantly enriched on promoters and exons, whereas the more accessible regions are significantly depleted on promoters and exons, and neither the less nor the more accessible DARs are significantly enriched with introns and intergenic regions (Figure 5C). Consistent with these findings, we observed that the less accessible regions are enriched for the promoter mark H3K4me3 as well as active marks such as H3K27ac and H3K23ac (Figures S5H and S5I). We found a significant concordance between the less accessible promoters and downregulated genes and globally observed that less accessible regions are predominantly localized to the A-compartment (Figures 5D and S5J; Tables S5D and S5E). The biological processes associated with these downregulated genes with reduced promoter accessibility includes cell cycle regulation, transcriptional regulation, mRNA splicing, and chromatin organization, the biological processes not associated with the 3D-genome reorganization (Figure S5K). While we observed a significantly higher number of more accessible regions genome-wide, this increased chromatin accessibility is not specific to any annotated genomic regions.

Motif analysis of the less accessible regions in T21 NPCs revealed significant enrichment of TF-binding motifs for SP1 (p value = $1e^{-44}$) and NFY (p value = $1e^{-41}$) (Figures 5E and 5F). NFY and SP1 are transcription factors involved in the regulation of cell cycle and proliferation (Benatti et al., 2011; Grinstein et al., 2002; Oh et al., 2007; Zhang et al., 2014b). While the accessibility of regions harboring the SP1 and NFY motifs is reduced, the transcript levels of SP1 and the different isoforms of NFY (NFYA, NFYB, and NFYC) remain unchanged in T21 NPCs (Figure S5L). The downregulated gene promoters with less accessible SP1 motifs are enriched for biological processes involved in cell cycle, gene expression regulation, RNA splicing, nucleosome assembly, and DNA damage response, whereas the downregulated genes with less accessible promoters harboring the NFY motifs are associated with transcriptional regulation, mRNA metabolic processes, and cellular senescence (Figures 5G and 5H). Overall, our findings indicate that the biological processes disrupted by T21 are driven by three disruptions in chromatin organization: (1) brain development-asso-

ciated downregulated genes are predominantly localized within reduced-ID TADs, (2) cell migration-associated upregulated genes are localized within increased-ID TADs, and (3) cell proliferation-, transcriptional regulation-, and chromosomal organization-related downregulated genes are associated with reduced promoter accessibility (Figures 4F, 4G, and S5K).

T21 induces NPC senescence

The global changes we observed in T21 NPCs including chromosomal introversion, disruption of LADs, and transcriptional and chromatin state changes have all been identified as key features of senescent cells (Criscione et al., 2016; Hernandez-Segura et al., 2017; Lenain et al., 2017; Parry et al., 2018; Sati et al., 2020; Zirkel et al., 2018). Senescence is a stress response that quenches the proliferative capacity of cells and is predominantly associated with cellular aging (Hayflick and Moorhead, 1961). To assess whether T21 NPCs undergo senescence, we performed senescence-associated (SA) β -galactosidase staining and observed an ~15-fold increase (p value = 0.001) in the number of senescent cells in T21 NPCs (Figures 6A and 6B; Table S6A). Additionally, we observed increased HP1-alpha and decreased HMGB1 and H3K27me3 levels, similar to what has been observed in senescent cells (Figures S6A and S6B; Table S6B) (Zirkel et al., 2018). To confirm that T21-NPCs do not undergo premature differentiation, we compared our RNA-seq data from iPSCs and NPCs with previously published data sets from iPSC-derived neurons and NPC-derived astrocytes and oligodendrocytes. We observed that euploid and T21 NPCs transcriptionally clustered together and were distinct from all other cell types (Figure S6C) (García-León et al., 2018; Lin et al., 2018; Tcw et al., 2017). Additionally, we stained for the astrocytic marker GFAP, a senescence marker p16^{INK4a}, and the intermediate filament marker vimentin. Vimentin staining indicated that euploid and T21 NPCs were morphologically distinct from astrocytes, and while NPC-derived astrocytes express GFAP, they are absent from both euploid and T21 NPCs, indicating that despite the elevated level of p16^{INK4a} in T21 NPCs, they do not undergo premature differentiation to astrocytes (Figures S6D and S6E).

To assess the transcriptional similarities between T21 and senescent cells, we utilized previously published transcriptomic data where senescence was induced through oxidative stress (oxidative stress-induced senescence [OSIS]), replicative stress (replicative senescence [RS]), radiation ionization (stress-induced premature senescence [SIPS]), overexpression of RAS (oncogene-induced senescence [OIS]), and HMGB2 knockdown (HMGB2-KD) (Alspach et al., 2014; Borràs-Fresneda et al., 2016; Casella et al., 2019; Crowe et al., 2016; Herranz et al., 2015; Marthandan et al., 2014; Nelson et al., 2016; Sati et al., 2020; Zirkel et al., 2018). Permutation test of DEGs identified in T21 iPSCs from our study (Iso-E and Iso-T) as well as from previously published data set (Gonzales et al., 2018) showed a lack of

(E) Venn diagram of overlapping downregulated (top) and upregulated (bottom) genes identified in NPCs harboring T21 and compared with DEGs identified in OSIS-induced senescent cells.

(F) Enrichment heatmap of the randomized permutation test between DEGs identified in both T21-NPCs and OSIS-induced senescent cells (SA-DEGs) with differential ID TADs as well as reduced promoter accessibility. Color intensity (positive correlations are displayed in green, and negative correlations in black) and the size of the circle are proportional to the enrichment coefficients.

(G and H) Gene ontology visualized in semantic similarity-based scatterplots for downregulated (G) and upregulated (H) overlapping genes identified in both T21-NPCs and OSIS-induced senescent cells.

correlation between DEGs identified in iPSCs and the various forms of senescence induction (Figure 6C; Tables S6C and S6D). In contrast, the DEGs identified in T21 NPCs (isogenic pair, female pair, and male pair) had the highest correlation compared with the DEGs identified in OSIS (p value $< 1 \times 10^{-07}$) and, to a lesser extent, with RS and SIPS. We found that T21 induced a marked expression increase of the SA cyclin-dependent kinase inhibitors (p16, p15, and p21), upregulation of SA secretory phenotype (SASP) genes (*CXCL12*, *MMP24*, *MMP25*, and *LAMB1*), and decreased expression of nuclear markers of senescence (*LMNB1*, *P53*, *HMGB1*, and *HMGB2*) similar to senescent cells induced through various mechanisms, particularly OSIS and RS (Figure 6D).

To identify the DEGs associated with senescence in T21 NPCs, we focused our analysis on the DEGs identified through OSIS. We observed a significant overlap (p value $< 1 \times 10^{-07}$) between DEGs identified in T21 NPCs and those in OSIS, where 426 genes were downregulated and 584 genes were upregulated in both (hereafter referred to as SA-DEGs; Figure 6E). Next, we performed an enrichment analysis of the SA-DEGs identified in T21 NPCs and identified a significant enrichment of SA-downregulated genes in reduced-ID TADs ($\log_2(\text{obs}/\text{exp}) = 1.17$, p value $< 1 \times 10^{-7}$), SA-upregulated genes in increased-ID TADs ($\log_2(\text{obs}/\text{exp}) = 0.62$, p value $< 1 \times 10^{-7}$), and a modest but significant enrichment ($\log_2(\text{obs}/\text{exp}) = 0.32$, p value = 0.00083) of SA-downregulated genes with less accessible promoters (Figure 6F; Table S6E). The SA-downregulated genes are predominantly involved in cell differentiation, proliferation, and chromosome organization, whereas the SA-upregulated genes are associated with cell migration, vesicle-mediated transport, and inflammatory response (Figures 6G and 6H). While the DEGs unique to T21 NPCs and OSIS seem to encode for cell-type-specific processes, there are also shared biological processes (Figures S6G–S6J). In summary, our findings indicate that T21 NPCs exhibit features of senescent cells, such as expression of senescent markers and a global transcriptional signature similar to OSIS.

Senolytics ameliorate the T21-induced phenotype in NPCs

Early clinical trials utilizing the senolytic drug DQ have shown positive results in ameliorating SA features in individuals with diabetic kidney disease (Hickson et al., 2019). Furthermore, studies indicate that senolytic drugs not only selectively remove senescent cells but also alleviate the transcriptional and heterochromatin architecture changes induced during senescence (Geng et al., 2019); however, the beneficial impact of senolytic drugs on T21-induced senescence was unexplored. The isogenic NPCs were treated with either DQ (400 nM of dasatinib and 15 μ M of quercetin) or vehicle (DMSO) for 5 days (Figure 7A). We observed that DQ treatment significantly reduced the elevated level of p16^{INK4a} observed in the vehicle-treated T21 NPCs to that observed in vehicle-treated euploid NPCs (ANOVA p value = 1.2×10^{-2}) (Figures 7B and 7C; Table S7A). Next, we interrogated the consequences of senolytic drugs on heterochromatin architecture in T21 NPCs (Figure 7D). We found that 5 days of DQ treatment restored the heterochromatin distribution, as measured by the co-localization of H3K9me3 and *LMNB1* (ANOVA p value = 4.7×10^{-3}) and *LMNB1* levels

(ANOVA p value = 2.4×10^{-4}) to similar levels observed in the euploid NPCs (Figures 7E and 7F; Tables S7B and S7C).

Subsequently, we sought to explore the impact of senolytic treatment on the transcriptome of T21 NPCs. RNA sequencing revealed that ~54% of the DEGs induced by T21 in NPCs were ameliorated after 5 days of DQ treatment (Figure S7A; Table S7D). Clustering of the DEGs identified 8 clusters: 2 clusters where gene expression was rescued to the same transcriptional levels as the euploid NPCs (clusters I and II), 2 clusters where gene expression changes were mitigated (clusters III and IV), 2 clusters with *de novo* transcriptional changes (clusters V and VI), and 2 clusters that remained unchanged after DQ treatment (clusters VII and VIII) (Figure 5G). The *de novo* upregulated genes (cluster VI) represent a small percentage of the transcriptional changes induced by DQ treatment (<9%) and include a transcriptional response to the antioxidant activity of quercetin as well as neuronal apoptosis in response to the senolytic activity of DQ-T21 NPCs exhibited a significant increase in apoptotic cells after 6 h of DQ treatment (p value = 0.0004) (Figure S7B; Table S7E).

We also observed amelioration of a significant number of genes associated with cell cycle regulation upon DQ treatment of T21 NPCs (cluster III). Notably, cell cycle dysfunction during neurodevelopment is a hallmark of DS (Contestabile et al., 2009; Contestabile et al., 2007). To examine cell cycle dynamics in T21 NPCs, we utilized a 2-h BrdU incorporation to label newly replicated/synthesized DNA (a marker of S-phase cells) coupled with Ki-67 staining, a marker of all cycling cells irrespective of cell cycle phase (Figures S7C and S7D). After DQ treatment of trisomic NPCs, the proportion of proliferative (Ki-67⁺ and SOX1⁺) NPCs was rescued to the same levels as euploid NPCs (Iso-E(veh) = 62.1%, Iso-T(veh) = 44.9% and Iso-T(DQ) = 73.1%, ANOVA p value = 2.9×10^{-3}) (Figure S7E; Table S4I). Furthermore, analysis of the NPCs that have traversed through S-phase (BrdU⁺ and SOX1⁺) in the 2-h BrdU incorporation window showed that cycling T21 NPCs led to significant reduction in S-phase cells (Iso-E(veh) = 25.3% and Iso-T(veh) = 13.4%, Tukey's $\text{padj} < 1.0 \times 10^{-4}$), similar to what has previously been observed in the developing brain of individuals with DS (Figure S7F; Table S7F), which was rescued to euploid levels upon DQ treatment (Iso-T(DQ) = 26.7%, Tukey's $\text{padj} = 1.0 \times 10^{-4}$).

Additionally, senolytic treatment rescued the levels of upregulated genes and resulted in *de novo* downregulation of genes involved in ECM organization, cell adhesion and cell migration in T21 NPCs (clusters II and V, respectively; Figure 7G). Thus, we explored the impact of senolytic treatment on the migratory abilities of T21 NPCs, a process disrupted in DS as well as in senescent cells (Huo et al., 2018; Romanov et al., 2010) by treating the isogenic pair of NPCs with either vehicle or DQ for 5 days in a monolayer culture system (Figure S7G). Next, NPCs were allowed to self-aggregate into neurospheres for an additional 5 days without vehicle or DQ (day 5–10), before embedding them into 3D-Matrigel scaffold (Figure S7H). After 3 days (day 13), the embedded neurospheres were stained for the NPC marker SOX1, and the number of migratory cells as well as the distance traveled by each cell from the edge of the neurosphere were assessed (Figure S7I). We found that DQ treatment of T21 NPCs rescued both the average number of migratory cells per neurosphere (ANOVA p value $< 1.0 \times 10^{-4}$) as well as the

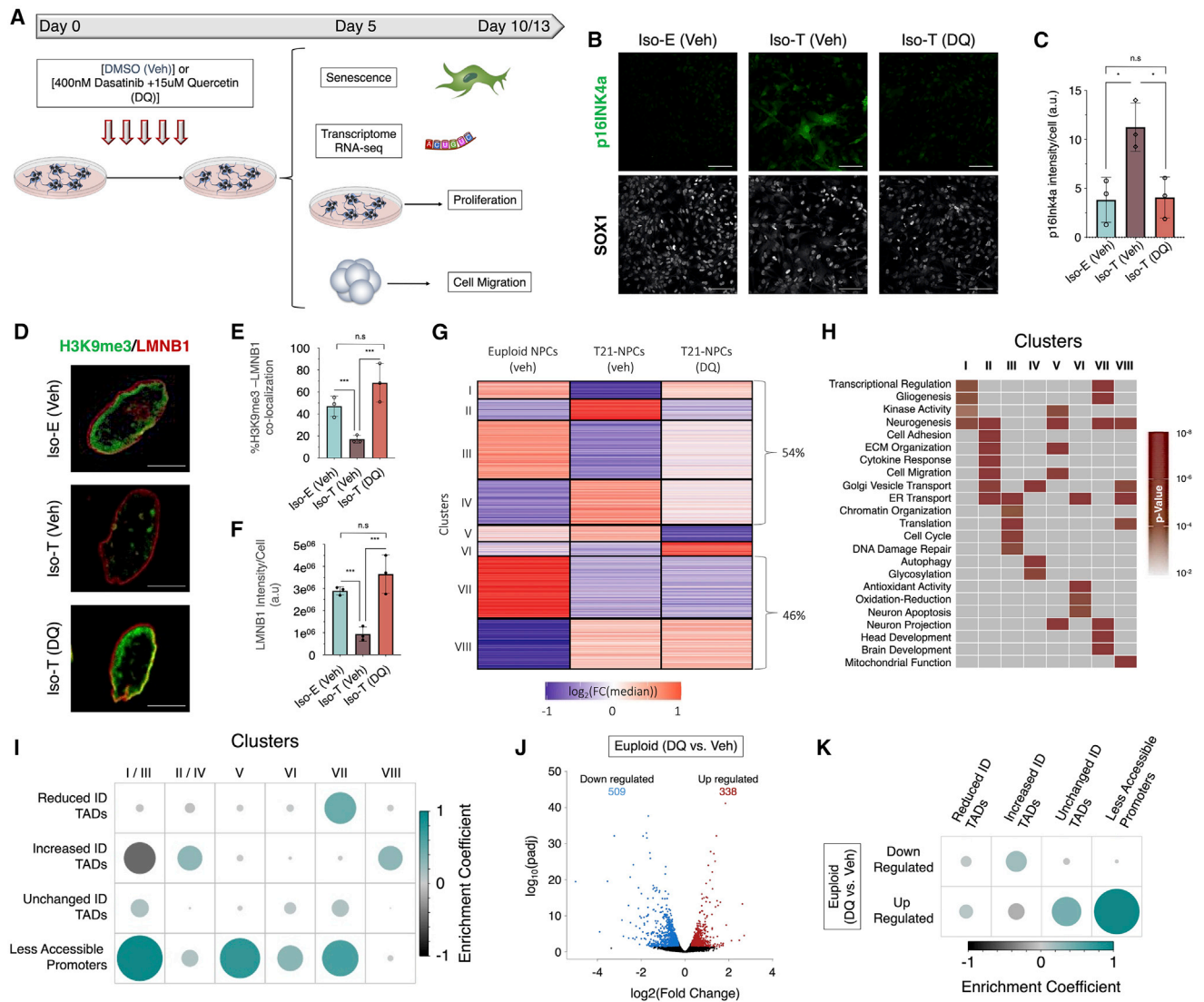


Figure 7. Senolytic drug alleviates the transcriptional and cellular dysfunctions induced by T21 in NPCs

(A) Schematic of DQ treatment experimental design in isogenic T21 NPCs.
 (B and C) Immunofluorescence (B) and quantification (C) of p16^{INK4a} (green) in euploid (Iso-E) and T21 (Iso-T, vehicle or DQ) NPCs (ANOVA).
 (D) Immunofluorescence of H3K9me3 (green) and LMNB1 (red) in euploid (Iso-E) and T21 (Iso-T, vehicle or DQ) NPCs.
 (E and F) Quantification of co-localization between H3K9me3 and LMNB1 (E) and LMNB1 staining intensity (F) in euploid (Iso-E) and T21 (Iso-T, vehicle or DQ) NPCs. Each dot on the histogram represents a replicate, and ~200 nuclei were analyzed per condition (ANOVA).
 (G) K-means clustering of the transcriptomic analysis of euploid and T21 NPCs (vehicle or DQ) identified in 8 distinct clusters. Values in heatmap are plotted as the log₂-fold change from the median.
 (H) Gene ontology of biological process associated with the 8 transcriptional clusters identified in response to senolytic drug treatment.
 (I) Enrichment plot of the randomized permutation test between the genes identified in the 8 different clusters with differential ID TADs as well as less accessible promoters. Genes from cluster I and III as well clusters II and IV were merged for this analysis. Color intensity (positive correlations are displayed in green, and negative correlations in black) and the size of the circle are proportional to the enrichment coefficients.
 (J) Volcano plots of the differentially expressed genes (DEGs) identified in euploid NPCs treated with vehicle (DMSO) or DQ.
 (K) Enrichment plot of the randomized permutation test between DEGs identified in DEGs identified after DQ treatment with differential ID TADs as well as reduced promoter accessibility. Color intensity (positive correlations are displayed in green, and negative correlations in black) and the size of the circle are proportional to the enrichment coefficients.

average distance migrated by NPCs away from the edge of the neurosphere (ANOVA p value < 1.0 × 10⁻⁴) (Figures S7J and S7K; Table S7G).

Next, we sought to characterize the genes impacted by senolytic treatment in terms of chromatin accessibility and

TAD organization. We identified that the genes downregulated in T21 NPCs and upregulated by DQ (clusters I and III) are enriched for the genes with reduced promoter accessibility (log₂(-obs/exp) = 1.28, p value < 1 × 10⁻⁷), whereas T21-upregulated genes that were downregulated after DQ treatment (clusters II

and IV) are predominantly localized in increased-ID TADs ($\log_2(\text{obs}/\text{exp}) = 0.37$, p value $< 1 \times 10^{-7}$) (Figure 7I; Table S7H). The *de novo* downregulated (cluster V) and upregulated (cluster VI) genes after DQ treatment were both enriched for genes with reduced promoter accessibility in T21 NPCs. Upregulated genes identified in T21 NPCs that remained upregulated after DQ treatment (cluster VIII) were localized in increased-ID TADs ($\log_2(\text{obs}/\text{exp}) = 0.42$, p value $< 1 \times 10^{-7}$), whereas the downregulated genes that were not impacted by DQ (cluster VII) were enriched in reduced-ID TADs ($\log_2(\text{obs}/\text{exp}) = 0.71$, p value $< 1 \times 10^{-7}$) and genes with less accessible promoters ($\log_2(\text{obs}/\text{exp}) = 0.8$, p value $< 1 \times 10^{-7}$). Moreover, we observed that ~20% of downregulated (clusters I/III) and ~30% of upregulated genes (clusters II/IV) ameliorated by senolytic drug treatment are SA-DEGs (Figure S7L). The ameliorated SA-DEGs are involved in biological processes predominantly associated with cell cycle regulation (clusters I/III) and cell migration (clusters II/IV).

To interrogate whether senolytics directly impact the transcriptome of non-senescent cells, we treated euploid NPCs with DQ for 5 days and performed RNA-seq. We identified 338 upregulated and 509 downregulated genes in Iso-E NPCs treated with DQ (Figure 7J). We observed that the upregulated genes were predominantly enriched for biological processes associated with response to oxidative stress, which is expected because of the antioxidant activity of quercetin (Figure S7M). Conversely, we observed that many of the key biological processes associated with genes upregulated in T21 NPCs were downregulated in DQ-treated euploid NPCs, such as ECM organization, cell migration, cell differentiation, and chemotaxis (Figure S7N). Accordingly, DQ treatment of Iso-E NPCs significantly increased the average number of migratory cells per neurosphere as well as the average distance migrated by Iso-E NPCs away from the edge of the neurosphere (Figures S7J and S7K; Table S7G). Finally, we observed that DQ treatment of euploid NPCs induced downregulation of genes localized to increased-ID TADs in T21 NPCs ($\log_2(\text{obs}/\text{exp}) = 0.34$, p value $= 8.3 \times 10^{-5}$), the region of the genome that harbors many of the genes found to be upregulated in T21 NPCs (Figure 7J; Table S7I). In contrast, the genes upregulated in DQ-treated euploid NPCs were predominantly enriched in unchanged-ID TADs ($\log_2(\text{obs}/\text{exp}) = 0.4$, p value $< 1 \times 10^{-7}$) and in genes that exhibit reduced promoter accessibility in T21 NPCs ($\log_2(\text{obs}/\text{exp}) = 0.95$, p value $< 1 \times 10^{-7}$). In summary, senolytic drug treatment of T21 NPCs reduced the number of senescent cells, alleviated the heterochromatin architecture changes, ameliorated the genome-wide transcriptional disruption, mitigated the cell migration deficits, and increased the population of proliferative cells.

DISCUSSION

T21 impacts the brain development of nearly every individual with DS, and studies utilizing human-derived tissue samples and DS mouse models have established that T21 induces genome-wide transcriptional disruption (Bianco et al., 2016; Gonzales et al., 2018; Letourneau et al., 2014; Olmos-Serrano et al., 2016; Tyler and Haydar, 2013; Walus et al., 2016). However, the underlying molecular mechanisms contributing to an altered global transcriptional profile as a consequence of T21 were unknown. Here, we utilized human iPSCs and iPSC-derived NPCs to decode the molecular mechanisms underlying these

genome-wide transcriptional changes. While both iPSCs and NPCs exhibit a similar level of dosage-dependent transcriptional upregulation of a subset of expressed genes on HSA21, unexpectedly, we found that T21 has a distinct genome-wide impact on the transcriptome, epigenome, and 3D-genome of NPCs that is absent in iPSCs. Even though a cell-type-specific response to T21 is expected from the organ-specific etiologies observed in DS (Weijerman and de Winter, 2010), the mechanisms governing this cell-type-specific response remain unclear and require further studies to fully elucidate this distinct response to T21.

Globally, we observed chromosomal introversion in NPCs harboring T21, where every chromosome has reduced interactions with other chromosomes and increased self-interactions compared with euploid NPCs. Furthermore, this increase in chromosomal self-interactions occurs within TADs, where promoter-enhancer interactions are typically observed (Robson et al., 2019). In T21 NPCs, the chromosomal introversion is predominantly observed in regions of the genome associated with the nuclear lamina (B-compartment), and this feature is associated with disruption of LADs, which leads to intranuclear B-compartment bundles. In T21 NPCs, we find that the genome-wide transcriptional upregulation is enriched within TADs in the B-compartment that have increased chromosomal interaction densities. We find that the genes associated with specific biological processes disrupted in T21 NPCs are localized to distinct spatial genomic regions.

Recent studies have established the promising therapeutic potential of targeting senescent cells (Kirkland et al., 2017). Senolytic drugs not only eliminate senescent cells but also restore key cellular and molecular hallmarks associated with senescence (Geng et al., 2019; Head et al., 2012; Zhang et al., 2019). Chromosomal introversion and disruption of the nuclear lamina are key features of senescence (Criscione et al., 2016; Zirkel et al., 2018), and our analysis of three different individuals with DS revealed that T21 NPCs exhibit a transcriptional profile that resembles senescence and display several key SA phenotypes. We find that treating T21 NPCs with the senolytic drug DQ ameliorated the SA genome-wide transcriptional and heterochromatin architecture disruptions. Moreover, treatment with senolytics also restored the migratory and proliferative capacity in T21 NPCs, which are hallmark dysfunctions of the developing brain in individuals with DS (Chakrabarti et al., 2007; Contestabile et al., 2007, 2009).

In summary, our findings indicate that senescence may play a key role in the neurodevelopmental pathogenesis of DS, and we show that senolytics provide an exciting therapeutic avenue for treating individuals with DS by restoring NPC dysfunctions induced by T21.

Limitations of study

The iPSCs and NPCs generated for this study originated from individuals who passed away at a very young age, indicating the severity of trisomy 21 in these individuals, and thus, samples derived from older or live individuals may yield a milder phenotype than what has been described in this study. There are currently several approaches for generating iPSCs and NPCs, as well as identifying chromatin accessibility, LADs, and spatial chromatin organization, and thus, utilizing these different approaches or sampling at different time points may yield varying results to those

described in this article. While we compared NPCs derived from both male and female patients, the relatively small number of patients sampled also represents a limitation of our study. Furthermore, patient iPSCs and iPSC-derived NPCs are a valuable tool to model the neurodevelopmental aspects of DS *in vitro*; however, they may not fully recapitulate *in vivo* disease pathogenesis.

STAR★METHODS

Detailed methods are provided in the online version of this paper and include the following:

- **KEY RESOURCES TABLE**
- **RESOURCE AVAILABILITY**
 - Lead contact
 - Materials availability
 - Data and code availability
- **EXPERIMENTAL MODEL AND SUBJECT DETAILS**
 - Induced pluripotent stem cell (iPSC) generation and neural progenitor cell (NPC) differentiation
- **METHOD DETAILS**
 - Immunofluorescence imaging and analysis
 - Global Chromatin Profiling (GCP)
 - Library preparation and analysis
- **QUANTIFICATION AND STATISTICAL ANALYSIS**

SUPPLEMENTAL INFORMATION

Supplemental information can be found online at <https://doi.org/10.1016/j.stem.2021.12.002>.

ACKNOWLEDGMENTS

This work was supported by grants from the Alana foundation (received by L.-H.T.), the LuMind Foundation (received by H.S.M.), Burroughs Wellcome Fund (received by H.S.M.), UNCF-Merck postdoctoral fellowship (received by H.S.M.), and the National Institute of Health (3U54HG008097-05S1, received by J.D.J. and L.-H.T.). We would like to thank Dr. Jay Penney, Dr. Scarlett Barker, Dr. Matheus Victor, Dr. Ravikiran Raju, Dr. Priyanka Narayan, Dr. Ping-Chieh Pao, Dr. Emily Niederst, and the members of Tsai Lab for all the constructive discussions and feedback on the manuscript. We would also like to thank Ying Zhou and Dr. Jennie Young of the Tsai Lab, as well as Dr. Stuart Levine and his entire team at the MIT BioMicro Center. We would also like to thank Dr. Stuart Orkin for sharing the isogenic pair iPSCs utilized in this manuscript. We would also like to acknowledge that cartoon illustrations were created with [BioRender.com](https://www.biorender.com).

AUTHOR CONTRIBUTIONS

H.S.M. and L.-H.T. conceptualized and designed the project. H.S.M. and T.K. generated iPSCs and NPCs. H.S.M., E.R.L., G.Y.A., and L.N.G. performed cell culture experiments. H.S.M., L.A.W., E.R.L., G.Y.A., L.N.G., and F.A. performed immunostaining, imaging, and IMARIS analysis. H.S.M., E.R.L., G.Y.A., and S.R. performed RNA-seq experiments. H.S.M., A.M., E.R.L., and S.R. performed ATAC-seq library preparation. H.S.M. and S.R. performed Hi-C library preparation, and H.S.M. performed ChIP-seq library preparation and data analysis. H.S.M., A.M., and V.D. performed computational analysis. J.M. and M.P. performed global chromatin profiling experiments, and J.M. and H.S.M. performed data analysis. H.S.M., L.A.W., A.M., V.D., E.R.L., G.Y.A., J.M., M.P., and L.-H.T. wrote the manuscript with the input from all authors. L.-H.T. and J.D.J. provided the resources for the project.

DECLARATION OF INTERESTS

The authors declare no competing interests.

Received: May 10, 2020

Revised: August 30, 2021

Accepted: December 9, 2021

Published: January 6, 2022

REFERENCES

- Abdennur, N., and Mirny, L.A. (2020). Cooler: scalable storage for Hi-C data and other genomically labeled arrays. *Bioinformatics* 36, 311–316.
- Allis, C.D., and Jenuwein, T. (2016). The molecular hallmarks of epigenetic control. *Nat. Rev. Genet.* 17, 487–500.
- Alspach, E., Flanagan, K.C., Luo, X., Ruhland, M.K., Huang, H., Pazolli, E., Donlin, M.J., Marsh, T., Piwnica-Worms, D., Monahan, J., et al. (2014). P38MAPK plays a crucial role in stromal-mediated tumorigenesis. *Cancer Discov* 4, 716–729.
- Anders, S., Pyl, P.T., and Huber, W. (2015). HTSeq—a Python framework to work with high-throughput sequencing data. *Bioinformatics* 31, 166–169.
- Bally, B.P., Farmer, W.T., Jones, E.V., Jessa, S., Kacerovsky, J.B., Mayran, A., Peng, H., Lefebvre, J.L., Drouin, J., Hayer, A., et al. (2020). Human iPSC-derived Down syndrome astrocytes display genome-wide perturbations in gene expression, an altered adhesion profile, and increased cellular dynamics. *Hum. Mol. Genet.* 29, 785–802.
- Benatti, P., Dolfini, D., Viganò, A., Ravo, M., Weisz, A., and Imbriano, C. (2011). Specific inhibition of NF- κ B subunits triggers different cell proliferation defects. *Nucleic Acids Res* 39, 5356–5368.
- Benda, C.E. (1940). Growth disorder of the skull in mongolism. *Am. J. Pathol.* 16, 71–86.3.
- Bianco, K., Gormley, M., Farrell, J., Zhou, Y., Oliverio, O., Tilden, H., McMaster, M., and Fisher, S.J. (2016). Placental transcriptomes in the common aneuploidies reveal critical regions on the trisomic chromosomes and genome-wide effects. *Prenat. Diagn.* 36, 812–822.
- Borràs-Fresneda, M., Barquinero, J.F., Gomolka, M., Hornhardt, S., Rössler, U., Armengol, G., and Barrios, L. (2016). Differences in DNA repair capacity, cell death and transcriptional response after irradiation between a radiosensitive and a radioresistant cell line. *Sci. Rep.* 6, 27043.
- Buenrostro, J.D., Giresi, P.G., Zaba, L.C., Chang, H.Y., and Greenleaf, W.J. (2013). Transposition of native chromatin for fast and sensitive epigenomic profiling of open chromatin, DNA-binding proteins and nucleosome position. *Nat. Methods* 10, 1213–1218.
- Buenrostro, J.D., Wu, B., Chang, H.Y., and Greenleaf, W.J. (2015). ATAC-seq: A method for assaying chromatin accessibility genome-wide. *Curr. Protoc. Mol. Biol.* 109, 21–29, 1–21.29.9.
- Casella, G., Munk, R., Kim, K.M., Piao, Y., De, S., Abdelmohsen, K., and Gorospe, M. (2019). Transcriptome signature of cellular senescence. *Nucleic Acids Res* 47, 7294–7305.
- Chakrabarti, L., Galdzicki, Z., and Haydar, T.F. (2007). Defects in embryonic neurogenesis and initial synapse formation in the forebrain of the Ts65Dn mouse model of Down syndrome. *J. Neurosci.* 27, 11483–11495.
- Chambers, S.M., Fasano, C.A., Papapetrou, E.P., Tomishima, M., Sadelain, M., and Studer, L. (2009). Highly efficient neural conversion of human ES and iPS cells by dual inhibition of SMAD signaling. *Nat. Biotechnol.* 27, 275–280.
- Contestabile, A., Fila, T., Bartesaghi, R., and Ciani, E. (2009). Cell cycle elongation impairs proliferation of cerebellar granule cell precursors in the Ts65Dn mouse, an animal model for Down syndrome. *Brain Pathol* 19, 224–237.
- Contestabile, A., Fila, T., Ceccarelli, C., Bonasoni, P., Bonapace, L., Santini, D., Bartesaghi, R., and Ciani, E. (2007). Cell cycle alteration and decreased cell proliferation in the hippocampal dentate gyrus and in the neocortical germinal matrix of fetuses with Down syndrome and in Ts65Dn mice. *Hippocampus* 17, 665–678.
- Creech, A.L., Taylor, J.E., Maier, V.K., Wu, X., Feeney, C.M., Udeshi, N.D., Peach, S.E., Boehm, J.S., Lee, J.T., Carr, S.A., and Jaffe, J.D. (2015). Building the Connectivity Map of epigenetics: chromatin profiling by quantitative targeted mass spectrometry. *Methods* 72, 57–64.

- Criscione, S.W., De Cecco, M., Siranosian, B., Zhang, Y., Kreiling, J.A., Sedivy, J.M., and Neretti, N. (2016). Reorganization of chromosome architecture in replicative cellular senescence. *Sci. Adv.* *2*, e1500882.
- Crowe, E.P., Tuzer, F., Gregory, B.D., Donahue, G., Gosai, S.J., Cohen, J., Leung, Y.Y., Yetkin, E., Nativio, R., Wang, L.S., et al. (2016). Changes in the transcriptome of human astrocytes accompanying oxidative stress-induced senescence. *Front. Aging Neurosci.* *8*, 208.
- Dixon, J.R., Selvaraj, S., Yue, F., Kim, A., Li, Y., Shen, Y., Hu, M., Liu, J.S., and Ren, B. (2012). Topological domains in mammalian genomes identified by analysis of chromatin interactions. *Nature* *485*, 376–380.
- Dobin, A., Davis, C.A., Schlesinger, F., Drenkow, J., Zaleski, C., Jha, S., Batut, P., Chaisson, M., and Gingeras, T.R. (2013). STAR: ultrafast universal RNA-seq aligner. *Bioinformatics* *29*, 15–21.
- Down, J.L. (1995). Observations on an ethnic classification of idiots. 1866. *Ment. Retard.* *33*, 54–56.
- Dürbaum, M., Kuznetsova, A.Y., Passerini, V., Stingle, S., Stoehr, G., and Storchová, Z. (2014). Unique features of the transcriptional response to model aneuploidy in human cells. *BMC Genomics* *15*, 139.
- Eden, E., Navon, R., Steinfeld, I., Lipson, D., and Yakhini, Z. (2009). GOrilla: a tool for discovery and visualization of enriched GO terms in ranked gene lists. *BMC Bioinformatics* *10*, 48.
- Egan, B., Yuan, C.C., Craske, M.L., Labhart, P., Guler, G.D., Arnott, D., Maile, T.M., Busby, J., Henry, C., Kelly, T.K., et al. (2016). An alternative approach to ChIP-seq normalization enables detection of genome-wide changes in histone H3 lysine 27 trimethylation upon EZH2 inhibition. *PLoS One* *11*, e0166438.
- FitzPatrick, D.R., Ramsay, J., McGill, N.I., Shade, M., Carothers, A.D., and Hastie, N.D. (2002). Transcriptome analysis of human autosomal trisomy. *Hum. Mol. Genet.* *11*, 3249–3256.
- García-León, J.A., Kumar, M., Boon, R., Chau, D., One, J., Wolfs, E., Eggermont, K., Berckmans, P., Gunhanlar, N., de Vrij, F., et al. (2018). SOX10 single transcription factor-based fast and efficient generation of oligodendrocytes from human pluripotent stem cells. *Stem Cell Rep* *10*, 655–672.
- Geng, L., Liu, Z., Zhang, W., Li, W., Wu, Z., Wang, W., Ren, R., Su, Y., Wang, P., Sun, L., et al. (2019). Chemical screen identifies a geroprotective role of quercetin in premature aging. *Protein Cell* *10*, 417–435.
- Gonzales, P.K., Roberts, C.M., Fonte, V., Jacobsen, C., Stein, G.H., and Link, C.D. (2018). Transcriptome analysis of genetically matched human induced pluripotent stem cells disomic or trisomic for chromosome 21. *PLoS One* *13*, e0194581.
- Grinstein, E., Jundt, F., Weinert, I., Wernet, P., and Royer, H.D. (2002). Sp1 as G1 cell cycle phase specific transcription factor in epithelial cells. *Oncogene* *21*, 1485–1492.
- Guidi, S., Ciani, E., Bonasoni, P., Santini, D., and Bartesaghi, R. (2011). Widespread proliferation impairment and hypocellularity in the cerebellum of fetuses with down syndrome. *Brain Pathol* *21*, 361–373.
- Hawkins, R.D., Hon, G.C., Lee, L.K., Ngo, Q., Lister, R., Pelizzola, M., Edsall, L.E., Kuan, S., Luu, Y., Klugman, S., et al. (2010). Distinct epigenomic landscapes of pluripotent and lineage-committed human cells. *Cell Stem Cell* *6*, 479–491.
- Hayflick, L., and Moorhead, P.S. (1961). The serial cultivation of human diploid cell strains. *Exp. Cell Res.* *25*, 585–621.
- Head, E., Powell, D., Gold, B.T., and Schmitt, F.A. (2012). Alzheimer's disease in Down syndrome. *Eur. J. Neurodegener. Dis.* *1*, 353–364.
- Heinz, S., Texari, L., Hayes, M.G.B., Urbanowski, M., Chang, M.W., Givarkes, N., Rialdi, A., White, K.M., Albrecht, R.A., Pache, L., et al. (2018). Transcription elongation can affect genome 3D structure. *Cell* *174*, 1522–1536.e22.
- Hernandez-Segura, A., de Jong, T.V., Melov, S., Guryev, V., Campisi, J., and Demaria, M. (2017). Unmasking transcriptional heterogeneity in senescent cells. *Curr. Biol.* *27*, 2652–2660.e4.
- Herranz, N., Gallage, S., Mellone, M., Wuestefeld, T., Klotz, S., Hanley, C.J., Raguz, S., Acosta, J.C., Innes, A.J., Banito, A., et al. (2015). mTOR regulates MAPKAPK2 translation to control the senescence-associated secretory phenotype. *Nat. Cell Biol.* *17*, 1205–1217.
- Hickson, L.J., Langhi Prata, L.G.P., Bobart, S.A., Evans, T.K., Giorgadze, N., Hashmi, S.K., Herrmann, S.M., Jensen, M.D., Jia, Q., Jordan, K.L., et al. (2019). Senolytics decrease senescent cells in humans: preliminary report from a clinical trial of dasatinib plus quercetin in individuals with diabetic kidney disease. *EBioMedicine* *47*, 446–456.
- Huo, H.Q., Qu, Z.Y., Yuan, F., Ma, L., Yao, L., Xu, M., Hu, Y., Ji, J., Bhattacharyya, A., Zhang, S.C., and Liu, Y. (2018). Modeling Down syndrome with patient iPSCs reveals cellular and migration deficits of GABAergic neurons. *Stem Cell Rep* *10*, 1251–1266.
- Jaffe, J.D., Wang, Y., Chan, H.M., Zhang, J., Huether, R., Kryukov, G.V., Bhang, H.E., Taylor, J.E., Hu, M., Englund, N.P., et al. (2013). Global chromatin profiling reveals NSD2 mutations in pediatric acute lymphoblastic leukemia. *Nat. Genet.* *45*, 1386–1391.
- Kirkland, J.L., Tchkonja, T., Zhu, Y., Niedernhofer, L.J., and Robbins, P.D. (2017). The clinical potential of senolytic drugs. *J. Am. Geriatr. Soc.* *65*, 2297–2301.
- Klemm, S.L., Shipony, Z., and Greenleaf, W.J. (2019). Chromatin accessibility and the regulatory epigenome. *Nat. Rev. Genet.* *20*, 207–220.
- Lane, A.A., Chapuy, B., Lin, C.Y., Tivey, T., Li, H., Townsend, E.C., van Bodegom, D., Day, T.A., Wu, S.C., Liu, H., et al. (2014). Triplication of a 21q22 region contributes to B cell transformation through HMG1 overexpression and loss of histone H3 Lys27 trimethylation. *Nat. Genet.* *46*, 618–623.
- Langmead, B., and Salzberg, S.L. (2012). Fast gapped-read alignment with Bowtie 2. *Nat. Methods* *9*, 357–359.
- Lejeune, J., Gauthier, M., and Turpin, R. (1959). Human chromosomes in tissue cultures. *C. R. Hebd. Seances Acad. Sci.* *248*, 602–603.
- Lenain, C., de Graaf, C.A., Pagie, L., Visser, N.L., de Haas, M., de Vries, S.S., Peric-Hupkes, D., van Steensel, B., and Peepker, D.S. (2017). Massive reshaping of genome-nuclear lamina interactions during oncogene-induced senescence. *Genome Res* *27*, 1634–1644.
- Letourneau, A., Santoni, F.A., Bonilla, X., Sailani, M.R., Gonzalez, D., Kind, J., Chevalier, C., Thurman, R., Sandstrom, R.S., Hibaoui, Y., et al. (2014). Domains of genome-wide gene expression dysregulation in Down's syndrome. *Nature* *508*, 345–350.
- Li, H., and Durbin, R. (2009). Fast and accurate short read alignment with Burrows-Wheeler transform. *Bioinformatics* *25*, 1754–1760.
- Li, H., Handsaker, B., Wysoker, A., Fennell, T., Ruan, J., Homer, N., Marth, G., Abecasis, G., and Durbin, R.; 1000 Genome Project Data Processing Subgroup (2009). The Sequence Alignment/Map format and SAMtools. *Bioinformatics* *25*, 2078–2079.
- Lieberman-Aiden, E., van Berkum, N.L., Williams, L., Imakaev, M., Ragozky, T., Telling, A., Amit, I., Lajoie, B.R., Sabo, P.J., Dorschner, M.O., et al. (2009). Comprehensive mapping of long-range interactions reveals folding principles of the human genome. *Science* *326*, 289–293.
- Lin, Y.T., Seo, J., Gao, F., Feldman, H.M., Wen, H.L., Penney, J., Cam, H.P., Gjoneska, E., Raja, W.K., Cheng, J., et al. (2018). APOE4 causes widespread molecular and cellular alterations associated with Alzheimer's disease phenotypes in human iPSC-derived brain cell types. *Neuron* *98*, 1141–1154.e7.
- Litichevskiy, L., Peckner, R., Abelin, J.G., Asiedu, J.K., Creech, A.L., Davis, J.F., Davison, D., Dunning, C.M., Egertson, J.D., Egri, S., et al. (2018). A library of phosphoproteomic and chromatin signatures for characterizing cellular responses to drug perturbations. *Cell Syst* *6*, 424–443.e7.
- Liu, F., Wang, L., Perna, F., and Nimer, S.D. (2016). Beyond transcription factors: how oncogenic signalling reshapes the epigenetic landscape. *Nat. Rev. Cancer* *16*, 359–372.
- Love, M.I., Huber, W., and Anders, S. (2014). Moderated estimation of fold change and dispersion for RNA-seq data with DESeq2. *Genome Biol* *15*, 550.
- Lu, L., Chen, X., Sanders, D., Qian, S., and Zhong, X. (2015). High-resolution mapping of H4K16 and H3K23 acetylation reveals conserved and unique distribution patterns in Arabidopsis and rice. *Epigenetics* *10*, 1044–1053.
- Maclean, G.A., Menne, T.F., Guo, G., Sanchez, D.J., Park, I.H., Daley, G.Q., and Orkin, S.H. (2012). Altered hematopoiesis in trisomy 21 as revealed through *in vitro* differentiation of isogenic human pluripotent cells. *Proc. Natl. Acad. Sci. U. S. A.* *109*, 17567–17572.

- Marthandan, S., Priebe, S., Hemmerich, P., Klement, K., and Diekmann, S. (2014). Long-term quiescent fibroblast cells transit into senescence. *PLoS One* 9, e115597.
- McLaughlin, K., Flyamer, I.M., Thomson, J.P., Mjoseng, H.K., Shukla, R., Williamson, I., Grimes, G.R., Illingworth, R.S., Adams, I.R., Pennings, S., et al. (2019). DNA methylation directs polycomb-dependent 3D genome re-organization in naive pluripotency. *Cell Rep* 29, 1974–1985.e6.
- Moldrich, R.X., Dauphinot, L., Laffaire, J., Vitalis, T., Hérault, Y., Beart, P.M., Rossier, J., Vivien, D., Gehrig, C., Antonarakis, S.E., et al. (2009). Proliferation deficits and gene expression dysregulation in Down's syndrome (Ts1Cje) neural progenitor cells cultured from neurospheres. *J. Neurosci. Res.* 87, 3143–3152.
- Nelson, D.M., Jaber-Hijazi, F., Cole, J.J., Robertson, N.A., Pawlikowski, J.S., Norris, K.T., Criscione, S.W., Pchelintsev, N.A., Piscitello, D., Stong, N., et al. (2016). Mapping H4K20me3 onto the chromatin landscape of senescent cells indicates a function in control of cell senescence and tumor suppression through preservation of genetic and epigenetic stability. *Genome Biol* 17, 158.
- Nora, E.P., Lajoie, B.R., Schulz, E.G., Giorgetti, L., Okamoto, I., Servant, N., Piolot, T., van Berkum, N.L., Meisig, J., Sedat, J., et al. (2012). Spatial partitioning of the regulatory landscape of the X-inactivation centre. *Nature* 485, 381–385.
- Oh, J.E., Han, J.A., and Hwang, E.S. (2007). Downregulation of transcription factor, Sp1, during cellular senescence. *Biochem. Biophys. Res. Commun.* 353, 86–91.
- Olmos-Serrano, J.L., Kang, H.J., Tyler, W.A., Silbereis, J.C., Cheng, F., Zhu, Y., Pletikos, M., Jankovic-Rapan, L., Cramer, N.P., Galdzicki, Z., et al. (2016). Down syndrome developmental brain transcriptome reveals defective oligodendrocyte differentiation and myelination. *Neuron* 89, 1208–1222.
- Parry, A.J., Hoare, M., Bihary, D., Hänsel-Hertsch, R., Smith, S., Tomimatsu, K., Mannion, E., Smith, A., D'Santos, P., Russell, I.A., et al. (2018). NOTCH-mediated non-cell autonomous regulation of chromatin structure during senescence. *Nat. Commun.* 9, 1840.
- Pinter, J.D., Eliez, S., Schmitt, J.E., Capone, G.T., and Reiss, A.L. (2001). Neuroanatomy of Down's syndrome: a high-resolution MRI study. *Am. J. Psychiatry* 158, 1659–1665.
- Pombo, A., and Dillon, N. (2015). Three-dimensional genome architecture: players and mechanisms. *Nat. Rev. Mol. Cell Biol.* 16, 245–257.
- Raja, W.K., Mungenast, A.E., Lin, Y.T., Ko, T., Abdurrob, F., Seo, J., and Tsai, L.H. (2016). Self-organizing 3D human neural tissue derived from induced pluripotent stem cells recapitulate Alzheimer's disease phenotypes. *PLoS One* 11, e0161969.
- Ramírez, F., Bhardwaj, V., Arrigoni, L., Lam, K.C., Grüning, B.A., Villaveces, J., Habermann, B., Akhtar, A., and Manke, T. (2018). High-resolution TADs reveal DNA sequences underlying genome organization in flies. *Nat. Commun.* 9, 189.
- Ramírez, F., Ryan, D.P., Grüning, B., Bhardwaj, V., Kilpert, F., Richter, A.S., Heyne, S., Dündar, F., and Manke, T. (2016). deepTools2: a next generation web server for deep-sequencing data analysis. *Nucleic Acids Res* 44, W160–W165.
- Rao, S.S., Huntley, M.H., Durand, N.C., Stamenova, E.K., Bochkov, I.D., Robinson, J.T., Sanborn, A.L., Machol, I., Omer, A.D., Lander, E.S., and Aiden, E.L. (2014). A 3D map of the human genome at kilobase resolution reveals principles of chromatin looping. *Cell* 159, 1665–1680.
- Risso, D., Ngai, J., Speed, T.P., and Dudoit, S. (2014). Normalization of RNA-seq data using factor analysis of control genes or samples. *Nat. Biotechnol.* 32, 896–902.
- Robson, M.I., Ringel, A.R., and Mundlos, S. (2019). Regulatory landscaping: how enhancer-promoter communication is sculpted in 3D. *Mol. Cell* 74, 1110–1122.
- Romanov, V.S., Abramova, M.V., Svetlikova, S.B., Bykova, T.V., Zubova, S.G., Aksenov, N.D., Fornace, A.J., Jr., Pospelova, T.V., and Pospelov, V.A. (2010). p21(Waf1) is required for cellular senescence but not for cell cycle arrest induced by the HDAC inhibitor sodium butyrate. *Cell Cycle* 9, 3945–3955.
- Ross-Innes, C.S., Stark, R., Teschendorff, A.E., Holmes, K.A., Ali, H.R., Dunning, M.J., Brown, G.D., Gojis, O., Ellis, I.O., Green, A.R., et al. (2012). Differential oestrogen receptor binding is associated with clinical outcome in breast cancer. *Nature* 487, 389–393.
- Sati, S., Bonev, B., Szabo, Q., Jost, D., Bensadoun, P., Serra, F., Loubiere, V., Papadopoulos, G.L., Rivera-Mulia, J.C., Fritsch, L., et al. (2020). 4D genome rewiring during oncogene-induced and replicative senescence. *Mol. Cell* 78, 522–538.e9.
- Schoenfelder, S., and Fraser, P. (2019). Long-range enhancer-promoter contacts in gene expression control. *Nat. Rev. Genet.* 20, 437–455.
- Sheltzer, J.M., Torres, E.M., Dunham, M.J., and Amon, A. (2012). Transcriptional consequences of aneuploidy. *Proc. Natl. Acad. Sci. U. S. A.* 109, 12644–12649.
- Shevelyov, Y.Y., and Ulianov, S.V. (2019). The nuclear lamina as an organizer of chromosome architecture. *Cells* 8, 136d.
- Stagni, F., Giacomini, A., Emili, M., Guidi, S., and Bartesaghi, R. (2018). Neurogenesis impairment: an early developmental defect in Down syndrome. *Free Radic. Biol. Med.* 114, 15–32.
- Supek, F., Bošnjak, M., Škunca, N., and Šmuc, T. (2011). REVIGO summarizes and visualizes long lists of gene ontology terms. *PLoS One* 6, e21800.
- Tcw, J., Wang, M., Pimenova, A.A., Bowles, K.R., Hartley, B.J., Lacin, E., Machlovi, S.I., Abdelaal, R., Karch, C.M., Phatnani, H., et al. (2017). An efficient platform for astrocyte differentiation from human induced pluripotent stem cells. *Stem Cell Rep* 9, 600–614.
- Topol, A., Tran, N.N., and Brennand, K.J. (2015). A guide to generating and using hiPSC derived NPCs for the study of neurological diseases. *J. Vis. Exp.* 96, e52495.
- Tyler, W.A., and Haydar, T.F. (2013). Multiplex genetic fate mapping reveals a novel route of neocortical neurogenesis, which is altered in the Ts65Dn mouse model of Down syndrome. *J. Neurosci.* 33, 5106–5119.
- Walus, M., Kida, E., Rabe, A., Albertini, G., and Golabek, A.A. (2016). Widespread cerebellar transcriptome changes in Ts65Dn Down syndrome mouse model after lifelong running. *Behav. Brain Res.* 296, 35–46.
- Wangsa, D., Braun, R., Stuelten, C.H., Brown, M., Bauer, K.M., Emons, G., Weston, L.A., Hu, Y., Yang, H.H., Vila-Casadesús, M., et al. (2019). Induced chromosomal aneuploidy results in global and consistent deregulation of the transcriptome of cancer cells. *Neoplasia* 21, 721–729.
- Weick, J.P., Held, D.L., Bonadurer, G.F., 3rd, Doers, M.E., Liu, Y., Maguire, C., Clark, A., Knackert, J.A., Molinarolo, K., Musser, M., et al. (2013). Deficits in human trisomy 21 iPSCs and neurons. *Proc. Natl. Acad. Sci. U. S. A.* 110, 9962–9967.
- Weijerman, M.E., and de Winter, J.P. (2010). Clinical practice. The care of children with Down syndrome. *Eur. J. Pediatr.* 169, 1445–1452.
- Zhang, J.P., Zhang, H., Wang, H.B., Li, Y.X., Liu, G.H., Xing, S., Li, M.Z., and Zeng, M.S. (2014b). Down-regulation of Sp1 suppresses cell proliferation, clonogenicity and the expressions of stem cell markers in nasopharyngeal carcinoma. *J. Transl. Med.* 12, 222.
- Zhang, P., Kishimoto, Y., Grammatikakis, I., Gottmukkala, K., Cutler, R.G., Zhang, S., Abdelmohsen, K., Bohr, V.A., Misra Sen, J., Gorospe, M., and Mattson, M.P. (2019). Senolytic therapy alleviates Abeta-associated oligodendrocyte progenitor cell senescence and cognitive deficits in an Alzheimer's disease model. *Nat. Neurosci.* 22, 719–728.
- Zhang, Y., Liu, T., Meyer, C.A., Eickhout, J., Johnson, D.S., Bernstein, B.E., Nusbaum, C., Myers, R.M., Brown, M., Li, W., and Liu, X.S. (2008). Model-based analysis of ChIP-Seq (MACS). *Genome Biol* 9, R137.
- Zirkel, A., Nikolic, M., Sofiadis, K., Mallm, J.P., Brackley, C.A., Gothe, H., Drechsel, O., Becker, C., Altmüller, J., Josipovic, N., et al. (2018). HMGB2 loss upon senescence entry disrupts genomic organization and induces CTCF clustering across cell types. *Mol. Cell* 70, 730–744.e6.

STAR★METHODS

KEY RESOURCES TABLE

REAGENT or RESOURCE	SOURCE	IDENTIFIER
Antibodies		
OCT-4	Cell Signaling Technology	Cat# 2890, RRID:AB_2167725
Nanog	Cell Signaling Technology	Cat# 4893, RRID:AB_10548762
SOX1	R&D Systems	Cat# AF3369, RRID:AB_2239879
Nestin	Millipore Sigma	Cat# MAB5326, RRID:AB_2251134
PAX6	R&D Systems	Cat# AF8150, RRID:AB_2827378
H3K9me3	Abcam	Cat# ab176916, RRID:AB_2797591
HP1a	Cell Signaling Technology	Cat# 2616, RRID:AB_2070987
H3K27me3	Abcam	Cat# ab6002, RRID:AB_305237
HMGB1	Thermo Fisher Scientific	Cat# PA1-16926, RRID:AB_2248274
LMNB1	Abcam	Cat# ab16048, RRID:AB_10107828
p16INK4a	Thermo Fisher Scientific	Cat# MA5-32133, RRID:AB_2809424
KI-67	Abcam	Cat# ab15580, RRID:AB_443209
Vimentin	Abcam	Cat# ab24525, RRID:AB_778824
GFAP	Millipore	Cat# AB5804, RRID:AB_2109645
BrdU	Cell Signaling Technology	Cat# 5292, RRID:AB_10548898
Alexa-Fluor 488 (Donkey anti-Goat)	Thermo Fisher Scientific	Cat# A-11015, RRID:AB_2534082
Alexa-Fluor 488 (Donkey anti-Rabbit)	Thermo Fisher Scientific	Cat# A-21206, RRID:AB_2535792
Alexa-Fluor 488 (Donkey anti-Mouse)	Thermo Fisher Scientific	Cat# A-21202, RRID:AB_141607
Alexa-Fluor 488 (Donkey anti-Sheep)	Thermo Fisher Scientific	Cat# A-11015, RRID:AB_2534082
Alexa-Fluor 555 (Donkey anti-Goat)	Thermo Fisher Scientific	Cat# A-21432, RRID:AB_2535853
Alexa-Fluor 555 (Donkey anti-Rabbit)	Thermo Fisher Scientific	Cat# A-31572, RRID:AB_162543
Alexa-Fluor 555 (Donkey anti-Mouse)	Thermo Fisher Scientific	Cat# A-31570, RRID:AB_2536180
Alexa-Fluor 555 (Donkey anti-Sheep)	Thermo Fisher Scientific	Cat# A-21099, RRID:AB_2535753
Alexa-Fluor 647 (Donkey anti-Goat)	Thermo Fisher Scientific	Cat# A-21447, RRID:AB_2535864
Alexa-Fluor 647 (Donkey anti-Rabbit)	Thermo Fisher Scientific	Cat# A-31573, RRID:AB_2536183
Alexa-Fluor 647 (Donkey anti-Mouse)	Thermo Fisher Scientific	Cat# A-31571, RRID:AB_162542
Alexa-Fluor 647 (Donkey anti-Sheep)	Thermo Fisher Scientific	Cat# A-21448, RRID:AB_2535865
DAPI	Thermo Fisher Scientific	Cat# D1306, RRID:AB_2629482
Biological samples		
Iso-E and Iso-T iPSCs (AG05397)	Coriell (Maclean et al., 2012)	Cat# AG05397
Ma-E iPSCs	Cohen, McLean, HMS (Raja et al., 2016)	Cat# CS-0020-01
Ma-T Fibroblast	Coriell	Cat# AG06922
Fe-E iPSCs	WiCell	Cat# WA09
Fe-T Fibroblasts	Coriell	Cat# GM04616
CF1 Mouse embryonic fibroblasts, irradiated	Thermo Fisher Scientific	Cat# A34181
Chemicals, peptides, and recombinant proteins		
Fluoromount-G	Electron Microscopy Sciences	Cat# 17984-25
PBS, pH 7.4	Thermo Fisher Scientific	Cat# 10010049
Triton X-100	Sigma-Aldrich	Cat# T8787-100ML
Paraformaldehyde	Electron Microscopy Sciences	Cat# 15714-S
5-Bromo-2'-deoxyuridine	Sigma-Aldrich	Cat# B5002-5G
Corning® Matrigel® hESC-Qualified Matrix	VWR International	Cat# 354277

(Continued on next page)

Continued

REAGENT or RESOURCE	SOURCE	IDENTIFIER
Corning® Matrigel® Basement Membrane Matrix	VWR International	Cat# 356254
DMEM/F12 Glutamax	Life Technologies	Cat# 10565-042
Knockout Serum Replacement	Life Technologies	Cat# 10828028
MEM non-Essential amino acid solution	Sigma-Aldrich	Cat# M7145
Glutamax	Thermo Fisher Scientific	Cat# 35050-079
recombinant human FGF-basic	PeproTech	Cat# 100-18B
2-mercaptoethanol	Sigma-Aldrich	Cat# M6250
mTeSR1 medium	Stemcell technologies	Cat# 85850
ReLeSR™	Stemcell Technology	Cat# 05872
AggreWell™800	Stemcell Technology	Cat# 34811
Neurobasal	Thermo Fisher Scientific	Cat# 21103049
N-2 Supplement	Invitrogen	Cat# 17502-048
B-27 Serum-Free Supplement	Gibco	Cat# 12587010
insulin	Thermo Fisher Scientific	Cat# 41400045
Pen/strep	Gemini Bio-Products	Cat# 400-109
Dorsomorphin	PeproTech	Cat# 8666430
SB431542	Tocris	Cat# 1614
STEMdiff™ Neural Rosette Selection Reagent	Stemcell technologies	Cat# 05832
Sulfuric acid	Sigma-Aldrich	Cat# 339741-500ML
Trichloroacetic acid	BDH	Cat# BDH0310500G
Trypsin	Promega	Cat# V5113
C18 Sep-Pak cartridges	Waters	Cat# 186002318
TrypLE	Thermo Fisher Scientific	Cat# 12605028
Igepal CA-630 (NP-40)	Sigma-Aldrich	Cat# I8896
AMPure beads	Beckman Coulter	Cat# A63880
Critical commercial assays		
CytoTune-iPS Sendai Reprogramming kit	Thermofisher scientific	Cat# A16518
Kapa mRNA hyperprep kit for standard RNA libraries	Roche	Cat# KK8540
Nextera DNA Library Prep Kit	Illumina	Cat# FC-121-1030
Qiagen MinElute PCR Purification Kit	Qiagen	Cat# 28006
Arima Hi-C kit	Arima Genomics	N/A
Kappa Hyperprep Kit	Roche	Cat# KK8502
Deposited data		
Hi-C	This paper	GEO: GSE185192
LMNB1 ChIP-seq	This paper	GEO: GSE185192
RNA-seq	This paper	GEO: GSE185192
ATAC-seq	This paper	GEO: GSE185192
Senescence RNA-seq	Casella et al., 2019 ; Crowe et al., 2016 ; Alspach et al., 2014 ; Sati et al., 2020 ; Zirkel et al., 2018 ; Borras-Fresneda et al., 2016 ;	GEO: GSE130727, GSE58910, GSE56293, GSE130306, GSE98448, GSE80207
RNA-seq of iPSC derived from Down syndrome and control individuals	Gonzales et al., 2018	GEO: GSE101942
RNA-seq of iPSC derived neurons, astrocytes and OPCs	Garcia-Leon et al., 2018 ; Lin et al., 2018 ; Tcw et al., 2017	GEO: GSE106984, GSE102956, GSE97904
ChIP-seq of Histone Modifications	Hawkins et al., 2010	GEO: GSM956008
Experimental models: Cell lines		
Iso-E and Iso-T (AG05397)	Coriell (Maclean et al., 2012)	Cat# AG05397

(Continued on next page)

Continued		
REAGENT or RESOURCE	SOURCE	IDENTIFIER
Ma-E	Cohen, McLean, HMS (Raja et al., 2016)	Cat# CS-0020-01
Ma-T	Coriell	Cat# AG06922
Fe-E	WiCell	Cat# WA09
Fe-T	Coriell	Cat# GM04616
CF1 Mouse embryonic fibroblasts, irradiated	Thermo Fisher Scientific	Cat# A34181
Software and algorithms		
Imarisx64 9.2.1	Bitplane	http://www.bitplane.com/Default.aspx
ZEN imaging software	Carl Zeiss	https://www.zeiss.com/microscopy/int/products/microscope-software/zen.html
STAR (v.2.6.1a)	Dobin et al., 2013	https://github.com/alexdobin/STAR
HTSeq	Anders et al., 2015	https://htseq.readthedocs.io/en/master/
RUVSeq	Risso et al., 2014	https://bioconductor.org/packages/release/bioc/html/RUVSeq.html
DESeq2	Love et al., 2014	https://bioconductor.org/packages/release/bioc/html/DESeq2.html
Bowtie2	Langmead and Salzberg, 2012	http://bowtie-bio.sourceforge.net/bowtie2/index.shtml
Samtools	Li et al., 2009	http://samtools.sourceforge.net/
Homer		http://homer.ucsd.edu/homer/interactions2/index.html
MACS2.1.0	Zhang et al., 2008	https://github.com/taoliu/MACS
R		https://www.r-project.org/
Corrplot		https://github.com/taiyun/corrplot
Diffbind v1.16.3	Ross-Innes et al., 2012	https://bioconductor.org/packages/release/bioc/html/DiffBind.html
Burrows-Wheeler Aligner (BWA)	Li and Durbin, 2009	http://bio-bwa.sourceforge.net/
Juicer	Rao et al., 2014	https://github.com/aidenlab/juicer/wiki
Graphpad Prism 8	Graphpad	https://www.graphpad.com/
Distiller	Abdennur and Mirny, 2020	https://github.com/mirnylab/distiller-nf
Hi-C explorer	Ramirez et al., 2018	https://hicexplorer.readthedocs.io/en/latest/content/list-of-tools.html
BEDTools		https://bedtools.readthedocs.io/en/latest/
deepTools	Ramírez et al., 2016	https://deeptools.readthedocs.io/en/develop/

RESOURCE AVAILABILITY

Lead contact

Further information and requests for resources and reagents should be directed to and will be fulfilled by the lead contact, Li-Huei Tsai (lhtsai@mit.edu).

Materials availability

Unique resources and reagents generated in this study are available from the lead contact with a completed Material Transfer Agreement.

Data and code availability

Genomic sequencing data have been deposited at Gene Expression Omnibus (GEO) and are publicly available as of the date of publication. Accession numbers are listed in the key resources table. This paper does not report original code. Any additional information required to reanalyze the data reported in this paper is available from the lead contact upon request.

EXPERIMENTAL MODEL AND SUBJECT DETAILS

Induced pluripotent stem cell (iPSC) generation and neural progenitor cell (NPC) differentiation

iPSCs

The isogenic pair (Iso-E and Iso-T) of induced pluripotent stem cells (iPSCs) were provided by Dr. Stuart Orkin, Dana-Farber Cancer Institute, which have been described previously (Coriell, AG05397) (Maclean et al., 2012). The DS-iPSCs from the male individual (Ma-T, AG06922) purchased from Coriell and the female control iPSC (Fe-E, H9 WA09) purchased from WiCell. Fibroblasts of the derived from a female with DS, purchased from Coriell (GM04616) and fibroblasts from the male control (CS-0020-01) were utilized to generate iPSCs using Sendai virus to overexpress OCT4, SOX2, KLF4, and c-MYC, utilizing the CytoTune-iPS Sendai Reprogramming kit (ThermoFisher scientific, A16518) as previously described (Raja et al., 2016). iPSCs were cultured on irradiated mouse embryonic fibroblasts (MEFs, Thermo Fisher Scientific, A34181) in DMEM/F12 media supplemented with knockout serum replacement (KSR, 20% v/v), MEM non-Essential amino acid solution (Sigma-Aldrich M7145), Glutamax (Thermo Fisher Scientific 35050-079), 8 ng/μl recombinant human FGF-basic (FGF2, PeproTech, 100-18B) and 71.5 μM 2-mercaptoethanol (Sigma-Aldrich M6250). The quality of cells was monitored daily and differentiated cells were mechanically removed under a light microscope in a biosafety hood. iPSCs were cultured to 80% confluence and non-differentiated colonies were transferred to a feeder-free system and grown on Matrigel hESC-Qualified Matrix coated plates (VWR, 354277) using mTeSR1 medium (Stemcell technologies, 85850). iPSCs for RNA-seq, ATAC-seq, Hi-C and immunofluorescence imaging were grown under feeder-free conditions.

NPCs

NPCs were differentiated as previously described with minor adjustments (Chambers et al., 2009). iPSCs were grown to 80% confluence on feeder-free conditions in mTeSR1 medium. iPSCs were then dissociated into single cell suspension using ReLeSR™ (Stemcell Technology, 05872) following the manufacturers guidelines. 3 million cells were then transferred into a single well of AggreWell™800 (Stemcell Technology, 34811) to form 300 embryoid bodies of 10,000 iPSCs each in NPC-differentiation medium [1:1 of DMEM/F12 Glutamax and Neurobasal (Life Technologies 10565-042 and Thermo Fisher Scientific 21103049), N-2 Supplement (Invitrogen, 17502-048), B-27 Serum-Free Supplement (Gibco, 12587010), 2.5 μg/l insulin (Thermo Fisher Scientific, 41400045), Glutamax (Thermo Fisher Scientific, 35050-079), MEM non-Essential amino acid solution (Sigma-Aldrich, M7145), 71.5 μM 2-mercaptoethanol, Pen/strep (Gemini Bio-Products, 400-109), Dorsomorphin (PeproTech, 8666430) and SB431542 (Tocris, 1614)]. Half NPC-induction medium replacement was performed daily for 5 days and on day 6 EBs were washed and transferred onto Matrigel coated plates. Complete NPC-induction medium replacement was performed daily for 7 days, and on day 12 STEMdiff™ Neural Rosette Selection Reagent (Stemcell technologies, 05832) was utilized to isolate NPC-rosettes and re-plated on onto fresh Matrigel coated plates in NPC-induction medium. Complete NPC-induction medium replacement was performed for 7 days and on day 20 NPCs were transferred onto fresh Matrigel coated plates in NPC-expansion medium [1:1 of DMEM/F12 Glutamax and Neurobasal (Life Technologies 10565-042 and Thermo Fisher Scientific 21103049), N-2 Supplement (Invitrogen, 17502-048), B-27 Serum-Free Supplement (Gibco, 12587010), 2.5 μg/l insulin (Thermo Fisher Scientific, 41400045), Glutamax (Thermo Fisher Scientific, 35050-079), MEM non-Essential amino acid solution (Sigma-Aldrich, M7145), 71.5 μM 2-mercaptoethanol, Pen/strep (Gemini Bio-Products, 400-109) and 8 ng/μl recombinant human FGF-basic (FGF2, PeproTech, 100-18B)]. NPCs were passaged once a week and NPCs for RNA-seq, ATAC-seq, Hi-C, senolytic drug treatment and immunofluorescence imaging were used on passage 3-5.

METHOD DETAILS

Immunofluorescence imaging and analysis

iPSCs and NPCs grown on coverslips were fixed with 4% paraformaldehyde in 1X PBS for 15 minutes, then incubated overnight at 4°C in primary antibody in 1X PBS with 0.3% Triton X-100. Primary antibodies used were OCT-4 (CST C52G3), Nanog (CST 1E6C4), SOX1 (R&D Systems AF3369), Nestin (Millipore Sigma MAB5326), PAX6 (R&D Systems AF8150), H3K9me3 (Abcam 176916), LMNB1 (Abcam 16048), p16INK^{4a} (Thermo Fisher Scientific MA5-32133), KI-67 (Abcam 15580) and BrdU (CST 5292S) 1:500 dilution overnight at 40°C. Coverslips were washed three times with PBS and incubated with Alexa-Fluor 488, Alexa-Fluor 555 and/or Alex-Fluor 647 secondary antibodies (Thermo Fisher Scientific) 1:1,000 dilution, and DAPI (Invitrogen D1306) 1:5,000 dilution for two hours at room temperature. The coverslips were mounted on microscope slides with Fluoromount-G (Electron Microscopy Sciences 17984-25). The slides were imaged using a confocal microscope (LSM 710 and 880, Zeiss) with a 5X, 20x or 63x objective with identical settings for all matched images.

Heterochromatin architecture

iPSCs and NPCs grown on coverslips were fixed with 4% paraformaldehyde in 1X PBS for 12 minutes, then incubated overnight at 4°C in primary antibody in 1X PBS with 0.3% Triton X-100. Primary antibodies used were anti-LMNB1 (1:500) and anti-H3K9Me3 (1:1,000). Primary antibody targets were visualized with Alexa-Fluor 488 and Alex-Fluor 647 secondary antibodies, and cell nuclei were stained with DAPI. The coverslips were mounted on microscope slides with Fluoromount-G. The slides were imaged using a confocal microscope (LSM 880, Zeiss) with a 63x objective and identical settings were used for all coverslips. Images were quantified using ImaRISx64 9.2.1 (Bitplane, Zurich, Switzerland), to determine the number of heterochromatin aggregates (as labelled with H3K9Me3) and degree of co-localization with LMNB1 for the isogenic euploid, trisomic, and drug-treated trisomic cells. For each image, first, a “generous” surface was created on the LMNB1 staining and used to mask the H3K9Me3 channel, to eliminate general

extranuclear and background signal. The “generous” LMNB1 surface had surface detail of 0.6, the Imaris auto-generated surface threshold, and a volume gate of greater than 40 μm^3 . Then, a “stringent” LMNB1 surface was created, to hone in on the areas of the nuclei with the strongest LMNB1 signal. These “stringent” surfaces had surface detail of 0.2, surface threshold of 105, and no volume gate. Finally, spots were created on the H3K9Me3 channel, with diameter 0.65 μm and quality threshold 15.6. To quantify the co-localization, the “Find spots close to surface” command was used between the H3K9Me3 spots and the “stringent” LMNB1 surface, with a threshold of 0.35 μm . For each of the images, a total number was determined for both H3K9Me3 spots co-localized with LMNB1 and intra-nuclear H3K9Me3 aggregates.

Proliferation

NPCs were treated with 10 μM BrdU for 2hrs before fixing the cells with 4% paraformaldehyde in 1X PBS for 12 minutes. DNA hydrolysis was performed by treating NPCs with 1.5M HCl for 10mins at room temperature and washed 3x with 1X PBS. Cells were then permeabilized and primary antibodies was used against BrdU (1:500), KI-67 (1:1,000) and SOX1 (1:100). Primary antibody targets were visualized with Alexa-Fluor 488, Alexa-Fluor 555 and Alex-Fluor 647 secondary antibodies, and cell nuclei were stained with DAPI. The coverslips were mounted on microscope slides with Fluoromount-G. The slides were imaged using a confocal microscope (LSM 880, Zeiss) with a 20x objective and identical settings for all coverslips. Images were quantified using Imarisx64 9.2.1 (Bitplane, Zurich, Switzerland), to determine the proportion of proliferative NPCs. SOX1 surface were used to identify all the NPCs in the images with a setting of 0.75 μm surface grain size. Then BrdU and KI-67 positive cells under the SOX1 surface were quantified with a mean intensity of >18 and >10, respectively.

Cell Migration

Matrigel embedded neurospheres in 96-well glass bottom plates were fixed with 4% paraformaldehyde in 1X PBS for 15 minutes, then incubated overnight at 4°C in primary antibody in 1X PBS with 0.3% Triton X-100 with primary SOX1 (1:100) and Nestin (1:500). SOX1 was visualized with Alexa-Fluor 488 and Nestin was visualized with Alexa-Fluor 555 secondary, and nuclei were stained with DAPI. Fluoromount-G was then added onto Matrigel embedded neurospheres. The Matrigel embedded neurospheres were imaged using a confocal microscope (LSM 710, Zeiss) with a 5x objective and identical settings were used for all images. Images were then quantified using Imarisx64 9.2.1 (Bitplane, Zurich, Switzerland), to determine how far individual NPCs had migrated out of the neurospheres for the isogenic pair of euploid, trisomic and drug-treated trisomic neurospheres. For each image, first, a DAPI sphere surface was created to demarcate the boundaries of the neurosphere core. This surface had surface detail of 2, surface threshold of the Imaris auto-generated threshold divided by two, and a volume gate such that all but the largest surface is eliminated. Next, the DAPI sphere surface was used to mask the SOX1 channel, to isolate the signal from NPCs that had migrated out of the primary neurosphere. Finally, spots were created on the masked SOX1 channel, with diameter 15 μm and quality threshold 5. Then, the distance between the SOX1 spots and the DAPI sphere surface was calculated and a list of individual distance values for each migrated NPC was generated for each neurosphere.

Global Chromatin Profiling (GCP)

The Global Chromatin Profiling (GCP) assay was performed as previously described (Creech et al., 2015; Litichevskiy et al., 2018). Briefly, three biological and three technical replicates of neural progenitor cells (NPCs), derived from isogenic-pair (AG-005397 (iso-E and Iso-T)), were grown in 6-well plates, washed in ice cold PBS 2x, scraped, and collected by centrifugation. After nuclei were isolated using mild lysis conditions (0.3% NP40), histones were extracted using sulfuric acid (Sigma-Aldrich, 339741-500ML), and precipitated using trichloroacetic acid (BDH, BDH0310-500G). Samples (10 μg each) were propionylated, desalted and digested by trypsin (Promega, V5113) overnight following standard protocols. A second round of propionylation followed by desalting using C18 Sep-Pak cartridges (Waters, 186002318) was employed. A mix of isotopically labeled synthetic peptides for histone H3 was added as a reference to each sample prior to mass-spectrometric (MS) analysis. Peptides were separated on a C18 column (EASY-nLC 1000, Thermo Scientific) and analyzed by mass spectrometry (MS) in a parallel reaction monitoring mode (QExactiveTM Plus, Thermo Scientific) as previously described (Creech et al., 2015). Detailed protocols of sample preparation steps can be found in <https://panoramaweb.org/labkey/wiki/LINCS/Overview%20Information/page.view?name=sops>.

Library preparation and analysis

RNA-seq

Biological replicates (n=3) of the isogenic pair (Iso-E and Iso-T) of iPSCs and NPCs as well as the male (Ma-E and Ma-T) and female (Fe-E and Fe-T) pairs were used for library preparation. RNA quality was checked using RNA Integrity number on an Agilent Bio-analyzer 2100, and samples with a RIN score of >9 were used for library preparation. 150 ng of RNA was used to prepare libraries using the Kapa mRNA hyperprep kit for standard RNA libraries (Roche, KK8540) on a TecanEvo 150s (Tecan). >50 million 75-bp paired-end reads were acquired for each replicate using the NextSeq 500 platform at the MIT BioMicro Center. FASTQ paired-end reads were aligned using STAR (v.2.6.1a) to GRCh37 reference genome (GENCODE 19) (Dobin et al., 2013). Transcripts were quantified using HTSeq, data was normalized utilizing RUV-seq and differential gene expression analysis was performed through DESeq2 (Anders et al., 2015; Love et al., 2014; Risso et al., 2014). Significant differentially expressed genes (DEGs) were called with an FDR < 0.01, \log_2 fold change ≥ 0.5 or ≤ -0.5 . Gene ontology analysis was performed using *GORILLA with two unranked lists of genes (target and background lists) followed by REVIGO a program that can takes a long list of Gene Ontology terms and removes redundant GO terms and generates a scatterplot with an unbiased reduction of the GO terms in semantic space (x, y)* (Eden et al., 2009; Supek et al., 2011). Correlation analysis of the pairwise comparisons was performed using corplot

(<https://github.com/taiyun/corrplot>), utilizing the \log_2 fold overlap enrichment and significance p-value generated through randomized permutation test. Randomized permutation test was done in R using custom scripts. Briefly, a sample set of equal size as the observed data was randomly selected from the background set and then the statistic test was calculated for each randomly sampled data ($s^* = s_1, s_2, \dots, s_N$) exactly as for the observed data (sObs). This was iterated $N=10^7$ times with replacement to create the null distribution and the p-value was calculated using the formula.

$$p\text{-Value} = \text{sum}(s^* \geq \text{sObs}) / N \text{ (For enrichment)} \quad p\text{-Value} = 1 - \text{sum}(s^* \geq \text{sObs}) / N \text{ (For depletion)}$$

If sObs was greater than or less than all values in the null distribution, the p-value was set as $< < 1E-07$.

ChIP-seq

Libraries were generated from 2 million iPSC derived NPCs using the ChIP-IT® Express Kit and Sonication Shearing Kit (Active Motif) with Spike-in Chromatin from Drosophila (Active Motif) following to the manufacturer's instructions without any modifications (Egan et al., 2016). Briefly, the ChIP-seq library preparation consists of 8 steps: (i) cells were crosslinked with 1% formaldehyde, (ii) chromatin was sheared (Covaris E220 Focused-ultrasonicator) after lysing cells, (iii) digested chromatin was incubated with 2ug of LMNB1 antibody (Abcam, ab8982), samples were also incubated without any antibody for input and Spike-in chromatin was incubated with Spike-in antibody (Active motif). (iv) same amount of Spike-in chromatin/antibody was added to each sample. (v) antibody-bound DNA/protein complexes and input samples were captured and washed using Protein G magnetic beads. (vi) cross-links were reversed and protein was digested using proteinase K. (vii) DNA was purified utilizing QIAquick PCR Purification Kit (Qiagen, 28104) (viii) libraries were prepared utilizing the Kappa Hyperprep Kit (Roche, KK8502). Quality control was performed using the Agilent Bioanalyzer 2100. ~30 million 40-bp single-end reads were acquired for each replicate on the NextSeq 500 platform at the MIT BioMicro Center. FASTQ reads for each replicate were aligned using Bowtie 2.0 (bowtie2 -very-sensitive -k 30) to hg19 (human) and dm6 (drosophila) (Langmead and Salzberg, 2012). Samtools was used to sort (samtools sort), remove duplicates (samtools markdup), remove mitochondrial reads (samtools view) and index BAM files (samtools index) (Li et al., 2009). Bigwigs were generated from BAM files adjusted to the scale-factor for each sample using the percentage of mapped reads from the drosophila genome (dm6) to total reads over input utilizing deepTools (3.5.0) bamCoverage (Egan et al., 2016; Ramirez et al., 2016). Peak regions were identified using homer (4.11), with the function findPeaks utilizing the reads generated from input samples as background. Scatter plots and violin plots were generated utilizing the R package ggplot2.

ATAC-seq

Libraries were prepared as previously described (Buenrostro et al., 2015). 50,000 cells from the biological replicates ($n=3$) of the isogenic pair of iPSCs and NPCs were used for library preparation. Cells were harvested after treatment for 4 mins with ReLeSR™ (Stemcell Technology, 05872) for iPSCs and TrypLE (Thermo Fisher Scientific, 12605028) for NPCs were then counted and 50,000 cells were spun down at $500 \times g$ for 5 min, 4°C . Cells were with $50\mu\text{l}$ PBS and spun down at $500 \times g$ for 5 min, 4°C . Cells were then resuspended in fresh 50ul cold lysis buffer (0.15% igeal CA-630 (NP-40)) and left on ice for 10 min and spun down at $500 \times g$ for 5 min, 4°C . Next, tagmentation (Nextera FC-121-1030, Illumina) was carried out in 50ul volume ($25\mu\text{l}$ TD, $2.5\mu\text{l}$ TDE1, $22.5\mu\text{l}$ nuclease-free water), for 30 min at 37°C with gentle rocking. Transposed DNA fragments were purified using the Qiagen MinElute PCR Purification Kit (28006) and were barcoded, amplified (PCR reaction: 1 cycle; 5min at 72°C , 30sec at 98°C , 8 cycles; 15sec at 98°C , 30sec at 60°C , 3min at 72°C) and purified using AMPure beads (Beckman Coulter, A63880). ATAC-seq library fragment size distribution was assessed on an Agilent Bioanalyzer 2100. >50 million 40-bp paired-end reads were acquired for each replicate on the NextSeq 500 platform at the MIT BioMicro Center. FASTQ paired-end reads for each replicate were aligned using Bowtie 2.0 (bowtie2 -very-sensitive -k 30) to hg19 (Langmead and Salzberg, 2012). Samtools was used to sort (samtools sort), remove duplicates (samtools markdup), remove mitochondrial reads (samtools view), index BAM files (samtools index), and BAM files were shifted by +4bp and -5bp using an in-house algorithm (Li et al., 2009). Accessible chromatin peak calling was performed using Model-based Analysis of ChIP-Seq (macs2 callpeak -f BAMPE -g hs -q 0.05) (Zhang et al., 2008). Differential peaks analysis between the isogenic pairs was performed using Diffbind v1.16.3 (Ross-Innes et al., 2012). Correlation between differential accessibility of gene promoters ($-2,000\text{bp}$ and $+500\text{bp}$ of TSS) with differential expression was computed by first calculating the overlap percentage and significance of enrichment/depletion using a randomized permutation test then data was plotted as a histogram.

In situ Hi-C

Hi-C libraries were generated from 2 million iPSCs and NPCs using the Arima Hi-C kit (Arima Genomics, San Diego) following to the manufacturer's instructions without any modifications. Briefly, the Arima Hi-C kit consists of 6 steps: (i) cells were crosslinked with 1% formaldehyde, (ii) DNA was digested using the Arima restriction enzyme cocktail within intact permeabilized nuclei, (iii) ends were filled and biotinylated, (iv) blunt ends were ligated, (v) ligated fragments were purified, sheared and a biotin pull down was performed using streptavidin, and (vi) adapters were ligated, barcoded and amplified using the Kappa Hyperprep Kit (Roche, KK8502). Quality control was performed after shearing and library-prep using the Agilent Bioanalyzer 2100. Finally, >1.5 billion 40-bp paired-end reads were acquired for each replicate on the NextSeq 500 platform at the MIT BioMicro Center. FASTQ paired-end reads were processed through Juicer as previously described (Rao et al., 2014). In Brief, paired-end read pairs were aligned separately to the human genome (hg19) using BWA, then, duplicates/invalid pairs were removed, and the remaining reads were filtered based on mapping quality score of 30 (Li and Durbin, 2009). Interaction matrices were generated at resolutions of 2.5Mb, 1Mb, 500kb, 250kb, 100kb, 50kb, 25kb, 10kb, and 5kb and normalized interactions matrices were produced at all resolutions using Knight and Ruiz (`~/juicer/scripts/CPU/juicer.sh -D ~/juicer/ -y ~/juicer/restriction_sites/hg19_Arima.txt -s Arima`).

Trans-chromosomal interactions stats were generated through Juicer (Table S1) and a t-test was run comparing euploid and trisomic iPSCs and NPCs. Differential *trans*-interaction maps were generated through Hi-C Explorer utilizing the default setting (Ramirez et al., 2018). In brief, interaction matrices generated in juicer (.hic) were converted to cooler and then to h5 (hicConvertFormat -m matrix.hic -inputFormat hic -outputFormat cool -o matrix.cool -resolutions 1000000 -> hicConvertFormat -m matrix.cool -inputFormat cool -outputFormat h5 -o matrix.h5). Next, a matrix containing the normalized log2ratio values of trisomy/euploid was generated (hicCompareMatrices -m Trisomy.h5 Euploid.h5 -operation log2ratio -o Trisomy_Euploid.h5) and plotted (hicPlotMatrix -m Trisomy_Euploid.h5 -clearMaskedBins -vMin -1 -vMax 1 -o Trisomy_Euploid.png). Distribution of normalized counts was generated using distiller pipeline on nextflow (nextflow run distiller.nf -params-file project.yml) as previously described (<https://github.com/mirnylab/distiller-nf>) (Abdennur and Mirny, 2020). *Trans*-chromosomal interaction statistics generated by distiller was used to identify the distribution of the *trans*-chromosomal interaction for each chromosome and calculated as the percentage of total interactions per sample. A statistical t-test comparison of euploid and trisomic cells was performed for each chromosome after normalizing for the number of chromosomes, where all chromosomes were divided by 2 with the exception of chromosome 21 which was divided by two in euploid samples and divided by 3 in trisomic samples (Figure S1E; Table S3).

Cis-chromosomal interactions stats were generated through Juicer (Table S1) and a t-test was run comparing euploid and trisomic iPSCs and NPCs. Differential *trans*-interaction maps were generated using juicebox, and represents the foldchange of trisomic over euploid cells. Global decay plots were generated using an in-house algorithm. In brief, decay plots were made by plotting the "Fraction of total paired-end tags" vs "Distance between the paired-end tags" generated by homer Hi-C analysis pipeline (Heinz et al., 2018). Fold enrichment values for each distance intervals were calculated as $\log_2(\text{mean of trisomy replicates} / \text{mean of euploid replicates})$. The FDR p-values for the enrichment between the tree replicates for trisomy and disomy was calculated using t-test (two-tailed) and corrected using p.adjust function in the R library qvalue using standard methods (Benjamini & Hochberg). Short-range (<1Mb) to long-range (>1Mb) interaction ratios were generated using Hi-C explorer utilizing the default settings (hicPlotSVL -m Euploid_10kb.cool Trisomy_10kb.cool -distance 1000000) and a Wilcoxon rank-sum test was run between euploid and trisomic samples and represented as dot plots for each chromosome.

A/B compartments were analyzed utilizing the HOMER Hi-C analysis pipeline (<http://homer.ucsd.edu/homer/interactions2/index.html>) utilizing the default settings (Heinz et al., 2018). In brief, FASTQ paired reads were aligned separately using BWA (bwa mem -t8 -A1 -B4 -E50 -L0 ~/BWA_Index/hg19.fa), then tag directories were generated (makeTagDirectory sample_R1.sam, sample_R2.sam -tbp 1 -removePEbg -removeSpikes 10000 5). Principal component analysis of the Hi-C interaction matrices was used to reveal the active and inactive compartments of the genome (runHiCpca.pl auto sample_TagDir/ -res 25000 -window 50000 -genome hg19). Regions were annotated (annotatePeaks.pl) and edgeR/limma was used to identify the differential compartments (getDiffExpression.pl). Comparative analysis was performed to define the concordance between first principal component-based compartments identified through HOMER and the first principal component of the Pearson's matrix (eigenvector) identified through Juicer using bedtools intersect. Enrichment analysis with differentially expressed genes (DEGs) and differentially accessible regions (DARs) with A and B compartments was performed by first calculating the overlap percentage of DEGs and DARs with the different compartments and the significance of enrichment/depletion was calculated using a randomized permutation test (p-Value). Data was plotted as histogram or as corplot on R.

Loops and Topologically associating domains (TADs)

Loops were called using the default setting of HiCCUPS on juicer at 5Kb or 10Kb resolution (java -Xmx125g -jar ~/juicer/juicer_tools.jar hiccup). Differential looping between euploid and trisomic cells was identified using the default setting of HiCCUPS Diff on juicer using a graphics processing unit (GPU) (java -Xmx125g -jar ~/juicer/juicer_tools.jar hiccupsdiff). Aggregate plot analysis was performed using the APA command tool on juicer using the default settings (java -Xmx125g -jar ~/juicer/juicer_tools.jar apa) and genome-wide aggregate plots were generated from the normalized APA matrices on R. TADs boundaries, insulation scores and directionality index was computed using the default setting on HOMER (findTADsAndLoops.pl find TagDir/ -cpu 5 -res 3000 -window 15000 -genome hg19 -p badRegions.bed). For differential intra-tad interaction density analysis TAD files for the biological replicates per cell-type were merged (merge2Dbed.pl) and then interaction densities were quantified across replicates (findTADsAndLoops.pl score -tad). Finally, edgeR/limma was utilized to identify the differentially interacting TADs (getDiffExpression.pl). Enrichment analysis with differentially expressed genes was performed between down and upregulated genes with differentially interacting TADs and unchanged TADs, by first calculating the overlap percentage and significance of enrichment/depletion (randomized permutation test, p-Value). Data was plotted using corplot on R.

QUANTIFICATION AND STATISTICAL ANALYSIS

Data was analyzed using GraphPad Prism version 8. Replicate sizes and error bars definitions are indicated in the figure legends. Correct application of standard parametric procedures was confirmed and stated in the supplemental data. Two-tailed Student's t test were performed for datasets with two groups. ANOVA analyses were used for comparisons of data with more than two groups. Post hoc group comparisons were performed and stated in the figure legends and supplemental tables.

Differences were considered statistically significant at * ($p < 0.05$), ** ($p < 0.01$), *** ($p < 0.001$), and **** ($p < 0.0001$).